

AN ABSTRACT OF THE THESIS OF

David A. Dutton for the degree of Master of Science in Electrical and Computer Engineering presented on March 23, 2007

Title: Deep Ultraviolet Solid-State Laser Development

Abstract approved:

Thomas K. Plant

There is a new possibility of generating deep ultraviolet laser radiation from a solid-state source. With recent advances in material development, a new nonlinear optical crystal provides a greater damage threshold than current materials making higher conversion efficiencies possible.

This thesis examines the possibility of using this crystal to generate deep ultraviolet wavelengths. The best-estimated Sellmeier equations for this new crystal predict that direct doubling conversion using a 404 nm source is not possible. Observation of a 202 nm signal when the crystal is placed in front of a 404 nm source verifies the inaccuracy of the estimated Sellmeier equations. Additional verification of Sellmeier equations inaccuracy is provided when generation of 235 nm signal is found at an angle of 11 degrees less than the model prediction.

Possible electro-optic Q-switching is examined. Electro-optic modulation measurements show a very small refractive index change. When angle tuning, a

greater depth of modulation is noted, however, full extinction of the beam could not be achieved.

To improve efficiency, intra-cavity resonant doubling is investigated. Several cavity stabilization schemes are implemented successfully and compared. The cavity remains locked while being perturbed by outside forces and has less than 1% modulation on the signal under normal operating conditions.

Continued improvement in crystal quality will increase this crystal's production of UV light. This new material provides a solution for industrial solid-state deep ultraviolet laser sources.

©Copyright by David A. Dutton
March 23, 2007
All Rights Reserved

Deep Ultraviolet Solid-State Laser Development

by
David A. Dutton

A THESIS

submitted to

Oregon State University

in partial fulfillment of
the requirements for the
degree of

Master of Science

Presented March 23, 2007
Commencement June 2007

Master of Science thesis of David A. Dutton
presented on March 23, 2007.

APPROVED:

Major Professor, representing Electrical and Computer Engineering

Director of the School of Electric Engineering and Computer Science

Dean of the Graduate School

I understand that my thesis will become part of the permanent collection of Oregon State University libraries. My signature below authorizes release of my thesis to any reader upon request.

David A. Dutton, Author

ACKNOWLEDGEMENTS

The author expresses sincere appreciation for the following people who helped in the advancement of this project.

Thank you to Professor Mike Ramer and his graduate students at the University of Oregon for the use of his Ti-sapphire laser.

Thank you to Professor Wei Kong and her graduate students for the use of her dye laser at Oregon State University.

Thank you to Linsen Pei, a research associate working on his post doctorate for his help in dye concentration mixing, changing, and initial setup of the dye laser for our use.

Thank you to Mike Monroe, Ph.D., senior scientist at a local startup, for helping with mathematical calculations and determining the Sellmeier equations from phase matching angles.

Thank you to Theodore Alekel, Ph.D., chief technical officer at a local startup, for helping in the fundamental understanding and use of the new NLO material.

Thank you to Joseph G. LaChapelle, CEO of a local startup, for the use of equipment and use of the new NLO material.

Thank you to Professor Thomas K. Plant, an associate professor at Oregon State University, my advisor and mentor on this thesis.

Thank you, Priscilla K. Dutton, my wife, for your patience and understanding in this process.

Thank you to my Lord and savior Jesus Christ.

TABLE OF CONTENTS

	<u>Page</u>
1.0 Introduction.....	2
1.1. Thesis Objective.....	3
1.2. Thesis Organization.....	4
2.0 Background.....	6
2.1. Literature Review.....	6
2.1.1. Phase Matching.....	9
2.1.2. Modeling SHG.....	14
2.2. Possible NLO Materials.....	17
2.3. Current Deep UV Sources.....	20
2.4. Solid State Schemes for Deep UV	21
2.4.1. Single Pass.....	22
2.4.2. Linear Enhancement Cavity.....	23
2.4.3. Other Cavity Scheme.....	26
2.4.4. CW/Pulsed.....	27
2.5. IP04.....	28
3.0 n_e and n_o Sellmeier Equations.....	30
3.1. Experiments.....	30
3.2. Results.....	40
4.0 200 nm experiment.....	41
4.1. Experiments.....	41

TABLE OF CONTENTS (Continued)

	<u>Page</u>
4.2. Results.....	42
4.2.1. Second Harmonic Generation of 404 nm.....	43
4.2.2. Phase Matching Angles for 235 nm generation.....	44
4.2.3. Temperature Bandwidth.....	45
5.0 Electro-optic Measurements.....	46
5.1. Experiments.....	46
5.2. Results.....	56
6.0 Cavity Enhancement Control.....	58
6.1. Experiments.....	58
6.2. Results.....	61
7.0 Conclusions.....	67
7.1. Conclusions.....	67
7.2. Future Work.....	68
Bibliography.....	71
Appendix A.....	73

LIST OF FIGURES

<u>Figure</u>	<u>Page</u>
2.1 Illustration of (a) Positive uniaxial index ellipsoid, (b) negative uniaxial index ellipsoid.....	8
2.2 Visual illustration of the phase matching criteria required....	9
2.3 Normal surface plot for a type I conversion generating 532 nm.....	13
2.4 Systematic drawing of a lens focused onto a given crystal with beam dump and collimation optics.....	23
2.5 Schematic drawing model of a cavity with NLO material.....	24
2.6 Drawing modeling an enhancement cavity for generating 202 nm light.....	25
2.7 Optical schematic model illustration of a two cavity design using an 808 nm seed.....	26
3.1 Functional diagram of an Ellipsometer.....	31
3.2 IP04 n_e and n_o curves gathered from various data points.....	31
3.3 Indices for different materials.....	33
3.4 Indices for more different materials.....	36
4.1 202 nm spectrum data captured with an Ocean Optics Spectrometer.....	43

LIST OF FIGURES (Continued)

<u>Figure</u>	<u>Page</u>
5.1 Schematic drawing of the setup used for electro-optic modulation.....	47
5.2 Index ellipsoid cutaways with Ey field	52
5.3 Index ellipsoid cutaways with Ey field	54
5.4 Schematic drawing of the setup used to generate the second harmonic.....	55
5.5 Modulation of IP04 verses angle.....	57
6.1 Transmission spectrum of a cavity with a length of 45 mm, mirror one at 95% reflectance and mirror two at 98% reflectance.....	59
6.2 Error signal generated for a cavity with a length of 17.5 mm..	64
7.2 Cavity illustrations with coating specifications for laser mirrors.....	69

LIST OF TABLES

<u>Table</u>	<u>Page</u>
2.1 Uniaxial second harmonic phase-matching conditions.....	10
2.2 Comparison table of different crystal types.....	18
3.1 Wavelength mixing and phase matching angle chart.....	38
3.2 Wavelength mixing and phase matching chart to achieve 202 nm.....	39
3.3 Wavelength mixing and phase matching chart for 193 nm...	39
3.4 Wavelength mixing and phase matching using a 1550 nm source.....	40
6.1 Truth table of a sign switcher with a positive error signal....	65

Dedicated to the late Larry Alan Dutton

Deep Ultraviolet Solid-State Laser Development

by
David A. Dutton

1.0 INTRODUCTION

The first laser developed in the year 1960 used a ruby rod. The acronym “LASER” stands for Light Amplification by the Stimulated Emission Radiation. Today lasers are used in a wide variety of devices and applications. Devices including machining, fabrication, visualization, imaging, scanning, medicine, entertainment, military defense, and even kids spy toys. This small list gives an idea of just how common lasers are; every compact disc player uses a laser diode and a photodetector to read the data from tiny pits on the CD. Although ruby lasers are not widely used anymore due to their low quantum efficiency and pulsed-only operation, many other types of laser sources are used in our everyday lives.

The 1970's created a push, fueled by the fiber optics telecommunications industry, in the development and manufacturing of diode lasers. Laser diode costs depend on the power output and wavelength, but are much cheaper than other laser sources of the same power and wavelength. These devices, even with their vast diversity, still operate on the same principles used when the first ruby rod lased. The 1970's and 1980's created exciting development in short wavelength ultraviolet (UV) excimer lasers. Excimer lasers are gas lasers exciting diatomic molecules such as ArF and KrF into dissociative excited energy states allowing the short-lived states to emit light. Excimer lasers provide sources deeper in the UV spectrum, e.g. 193 nm and 248 nm.

Ultraviolet sources are some of the most advanced sources on the market. The current industrial markets for deep UV (wavelength <300 nm) include pulsed laser deposition (PLD), semiconductor lithography and machining. The short UV wavelengths allow for higher resolution lithography. However, resolving power comes at a cost. Extensive development efforts to make small affordable UV laser diodes for commercial use have recently led to InGaN₂ laser in the 320 nm – 400 nm near UV range. Deep UV devices have not yet been developed. The only high power solid-state deep UV sources are around 266 nm. This is achieved by either frequency doubling or mixing a pump laser using nonlinear crystals. Within the last few years, driven by the semiconductor industry, there has been a growing demand for deep ultraviolet solid-state lasers, [1]. This thesis describes experimental measurements of a new nonlinear optical (NLO) crystal candidate for solid-state, deep UV lasers.

1.1 Thesis Objective

Since the shortest current high power deep UV solid-state lasers wavelength are around 266 nm, it is important to explore other NLO crystals to push this limit to shorter wavelengths. This thesis explores a new crystal technology to extend the current deep UV wavelengths and extend the solid-state roadmap. This thesis also illustrates a design to drive the technology into an industrial application.

The ultimate objective of this thesis is to produce a deep ultraviolet, 202 nm diode-pumped laser. Currently several major corporations are eager to use solid-state deep UV constant wave (CW) or quasi CW sources. The application is for semiconductor process metrology. This thesis describes measurements of several fundamental crystal parameters to develop a CW 202 nm source with a few milli-watts of output power. Using the NLO crystal studied here, a high-powered 808 nm diode laser can be frequency doubled to 404 nm and then doubled again to 202 nm. This could be an effective and inexpensive source, since 808 nm diode lasers are readily available due to their use as a pump source for Nd:YAG, and Nd:YVO₄ lasers.

The desire to use this new technology as an intra-cavity-switchable-gain-medium requires knowledge of the unknown electro-optic coefficients and the spectral changes of the refractive index for the NLO crystal. Finally, to enhance the doubling efficiency it is necessary to control the NLO crystal inside a high Q resonant optical cavity. Several stable cavity control systems are presented.

1.2 Thesis Organization

Chapter two of this thesis discusses background topics for this work: second harmonic generation (SHG), possible NLO materials, current UV optical sources, schemes for UV production, and the new NLO material itself. Chapter three examines the topic of Sellmeier equations. Chapter four describes experiments

demonstrating 202 nm generation and the difference between theoretical and measured phase matching angles at 235 nm. Modulation measurements in chapter five indicate the value of the electro-optic coefficients. Control of the high Q resonant cavity in a CW system is discussed in chapter six. Chapter seven presents concluding remarks and topics for future work.

2.0 BACKGROUND

The development of a solid-state source at 202 nm requires careful investigation of available NLO materials, infrared fundamental frequency sources, and schemes to enhance and control the UV signal. This chapter will investigate each of these areas and outline a possible approach to achieve a deep UV solid-state source.

2.1 Literature Review

According to Photonics Dictionary, [2], second harmonic generation, (SHG) is, “a process whereby two fields of the same optical frequency interact in a nonlinear material to produce a third field, which has a frequency twice that of the two input fields.” The nonlinear optical (NLO) material described in the previous definition is typically a carefully oriented single crystal. Since crystals are dielectric materials, they also have given indices of refraction.

$$n = \sqrt{\varepsilon_r} , \quad (2.1.1)$$

where n is the index of refraction and ε_r is the relative dielectric constant in the optical range, [3]. Crystals can have two (uniaxial) or even three (biaxial) different axial indices of refraction. Current crystals used in SHG processes have low optical damage thresholds compared to a new crystal, studied for this thesis; which has a much higher damage limit that will allow deep ultraviolet solid-state production.

The nonlinear process of SHG involves matching the crystal's index of refraction at the fundamental laser wavelength to the index of refraction at the second harmonic laser wavelength generated, [4]. Uniaxial crystal structures, used for this process, can be classified as “negative” or “positive” uniaxial. In a positive uniaxial crystal the indices of refraction $n_x = n_y = n_o$ are less than $n_z = n_e$. n_o and n_e are called the ordinary and extraordinary index, respectively. For negative uniaxial crystals n_o is greater than n_e .

The index ellipsoids shown in Figure 2.1 below are for both types. The plot is a 3D surface showing the index of refraction for any direction in the crystal. Note that the x and y axis is n_o and the z-axis is n_e .

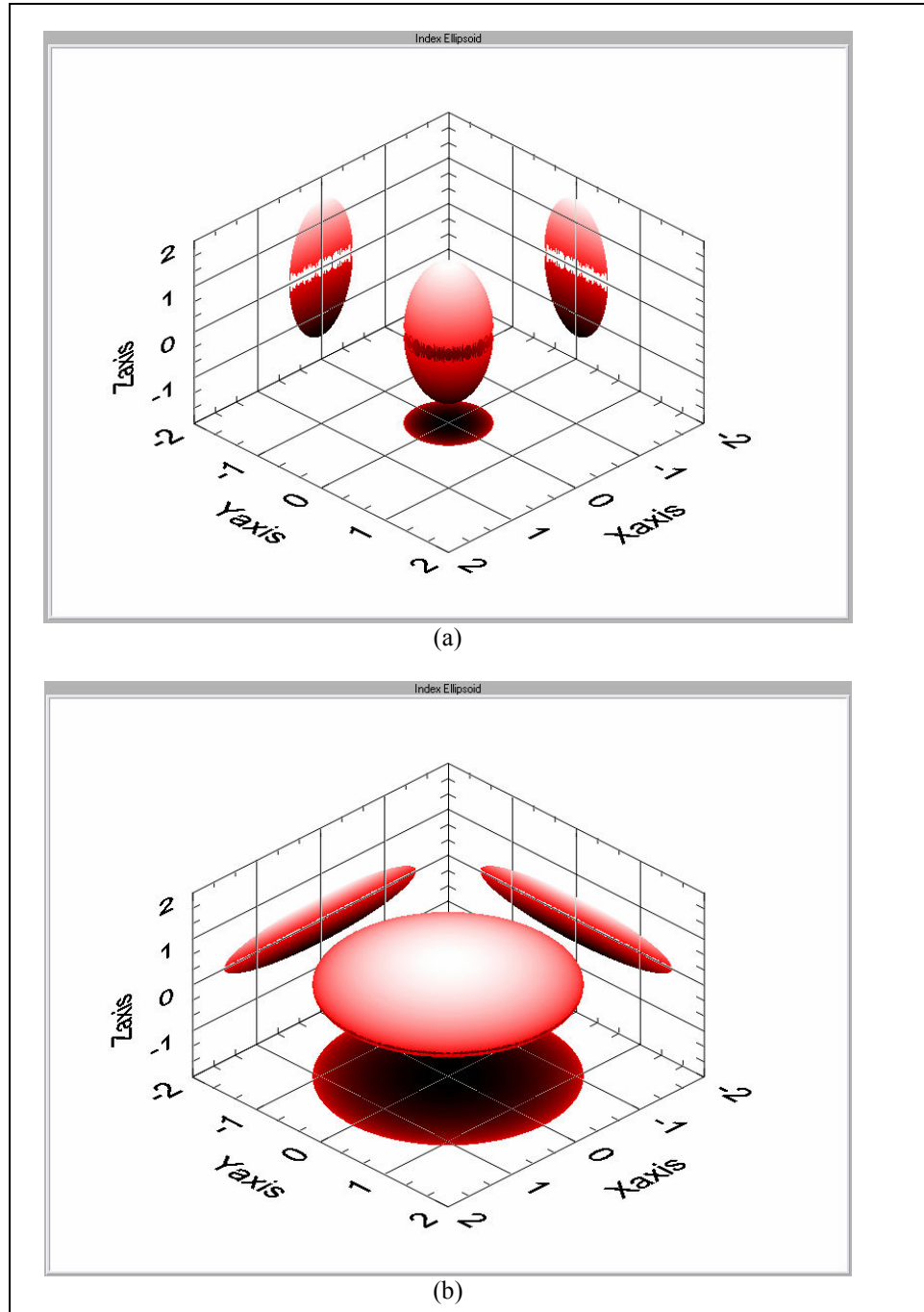


Figure 2.1. Illustration of (a) positive uniaxial index ellipsoid, and (b) negative uniaxial index ellipsoid. Note that pictures are exaggerated for visual viewing.

2.1.1 Phase Matching

Two different forms of second harmonic generation can take place. Type I involves two incoming photons with the same polarization whether that polarization is ordinary *or* extraordinary. Type II involves two incoming photons with different polarization ordinary *and* extraordinary. Figure 2.2 visually illustrates these polarization orientations needed to satisfy the indices requirements. Using the index of refraction at the different wavelengths determines the phase matching angle criteria. Table 2.1 best describes this process, [5]. “Phase matching” describes when energy is transferred from the fundamental optical frequency to twice the fundamental optical frequency traveling at the same velocity. This allows the coherent doubling process to build with the distance in the crystal.

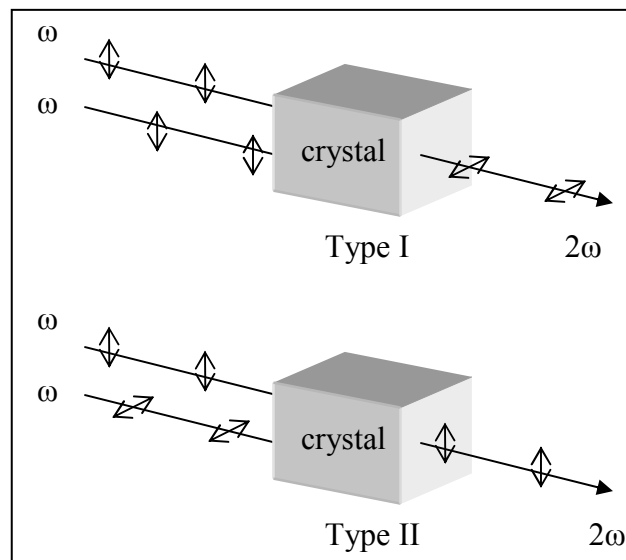


Figure 2.2. Visual illustration of the phase matching criteria required. Type I requires two of the same polarization orientation, while type II requires one of each.

Table 2.1 Uniaxial second harmonic phase-matching considerations.

	Positive Uniaxial	Negative Uniaxial
Type I	$n_{o_2} \cdot \omega_2 = 2 \cdot (n_{e_1} \cdot \omega_1)$	$n_{e_2} \cdot \omega_2 = 2 \cdot (n_{o_1} \cdot \omega_1)$
Type II	$n_{o_2} \cdot \omega_2 = n_{o_1} \cdot \omega_1 + n_{e_1} \cdot \omega_1$	$n_{e_2} \cdot \omega_2 = n_{e_1} \cdot \omega_1 + n_{o_1} \cdot \omega_1$

There are two common methods for phase matching. First consist of angle tuning, and the second consists of temperature tuning. One might do combinations of these methods. To achieve maximum angle tuning, approaching 90 degrees, it may be beneficial to use both methods depending upon the change in refractive index with temperature. Let us look at these methods each individually.

First, the phase matching angle is strongly dependent on the extraordinary index at the incoming angle. The angle referenced, is the propagation angle referenced from the C or Z-axis. Describing the extraordinary index to an incoming angle relates by the following equation, [5],

$$\frac{1}{n_e^2(\theta)} = \frac{(\sin(\theta))^2}{n_e^2} + \frac{(\cos(\theta))^2}{n_o^2}. \quad (2.1.2)$$

To find the phase matching condition for a type I process, solve Equation (2.1.2) for $n_e(\theta)$ which describes an extraordinary index at a particular angle. Insert $n_e(\theta)$ for n_e in the “Type I” line of Table 2.1. Through some manipulation the type I phase matching angle expression results in,

$$\theta = \sqrt{\arcsin\left(\frac{\frac{1}{(n_o(\omega))^2} - \frac{1}{(n_o(2\omega))^2}}{\frac{1}{(n_e(2\omega))^2} - \frac{1}{(n_o(2\omega))^2}}\right)}. \quad (2.1.3)$$

The same process can be used for type II phase matching using “Type II” in Table 2.1. Whether type I or type II phase matching conditions, both strongly depend on the angle of the crystal.

Secondly, temperature tuning requires the mapping of the index at each desired wavelength and its dependence on change in temperature. Similar to angle tuning, within the crystal there is a shift or change in the index of refraction allowing for phase matching condition achievement,[5]. From the Table 2.1, type I negative uniaxial phase-matching criteria, the new form is expressed as,

$$\omega_2 \cdot \left(n_{e_2}(T) + \frac{\partial n_{e_2}}{\partial T} \Delta T \right) = 2 \cdot \left(\omega_1 \cdot \left(n_{o_1}(T) + \frac{\partial n_{o_1}}{\partial T} \Delta T \right) \right) \quad (2.1.4)$$

The simplistic way to think of the new refractive index at a given temperature is the nominal value plus the change of index for the change in temperature.

Type II processes are a bit more challenging when determining the phase matching angle. No optics books clearly explain an analytical method of finding the phase matching angle. Determining a phase matching angle for a type II process can be done through an iterative approach. This can be done quickly and with few iterations. Using an evaluation tool like Excel, Equation (2.1.2) can be used to quickly evaluate the right hand side of the expression in the “Type II” line of Table 2.1. Other methods may include, but are not limited to, a graphical approach or root evaluation.

Taking an example with negative uniaxial beta-barium borate as our crystal material (materials discussed later) will illustrate the type I and type II phase matching angles. This example will use a 1064 nm infrared laser and convert it to a 532 nm green laser. Beta-barium borate has a refractive index n_o of 1.6545 and n_e of 1.5392 at 1064 nm. At 532 nm our crystal n_o is 1.6742 and n_e is 1.5546. Using Equation 2.1.3 we solve for a 22.8° type I phase matching angle. If you were to view the normal surface plot for this process the propagation angle is the intersection of the $n_e(\theta)$ and n_o surfaces at their appropriate frequencies. Figure 2.3 illustrates this concept. The normal incident crystal surface is orthogonal to the propagation axis. For a type II process, the phase matching angle is around 32.8° .

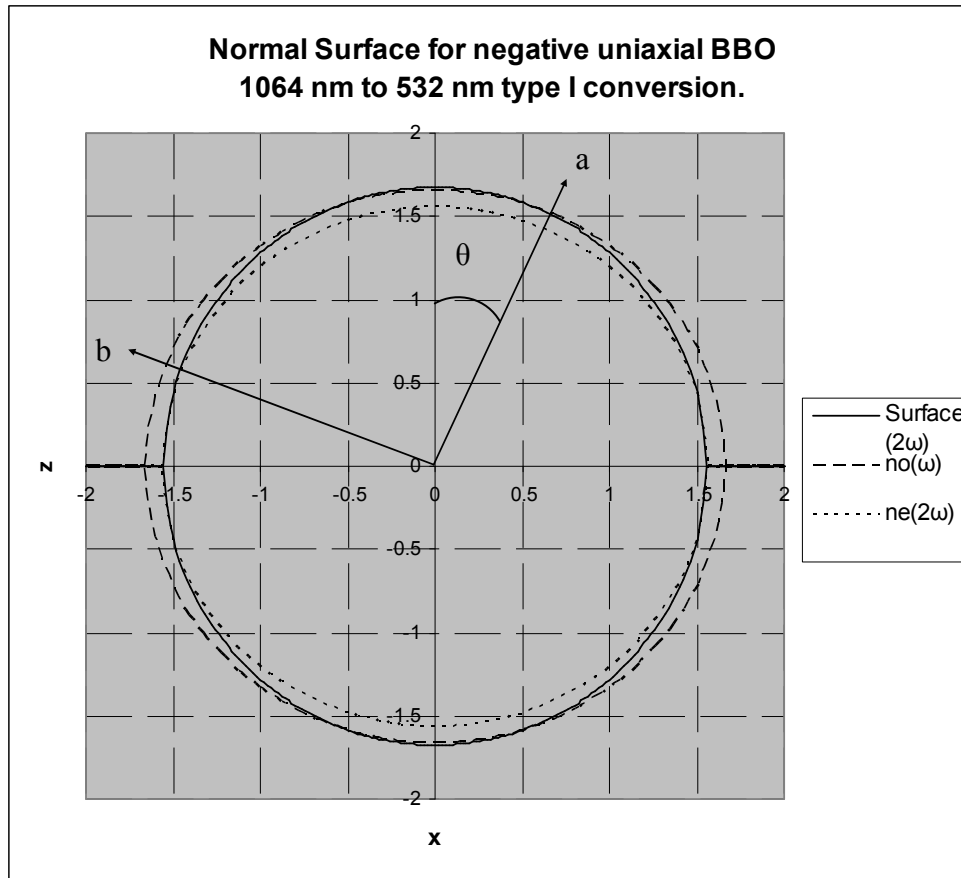


Figure 2.3. Normal surface plot for a type I conversion generating 532 nm. The “a” aligned arrow indicates propagation angle, 22.8° from the n_c , z, or c axis. Orthogonal to the phase matching vector “a” is the surface plane “b” vector.

Later this thesis will contain data on the indices of refraction for different types of materials. Comparing these materials’ indices of refraction with the new material under test, estimation of the indices will provide further insight into the solid-state development of 202 nm laser sources.

2.1.2 Modeling SHG

There are several different models in determining the second harmonic light generated from a nonlinear interaction, [6]. A non-depleted plane wave beam SHG approximation determines the power at the second harmonic through the following equation where

$$P(2\omega) = \frac{A \cdot L^2}{\pi \cdot w^2} \cdot P(\omega)^2, \quad (2.1.5)$$

and,

$$A = \frac{2 \cdot \omega^2 \cdot d_{eff}^2}{c_0^3 \cdot n^{2\omega} \cdot (n^\omega)^2 \cdot \epsilon_o}. \quad (2.1.6)$$

$n^{2\omega}$ and n^ω are the indices of refraction at the given light frequencies. L is the length of the crystal and ϵ_o is the permittivity in a vacuum. ω is the given light frequency and w is the waist (radius) of the beam. d_{eff} is a crystal-dependent term based on the nonlinear susceptibility tensor matrix. This will be discussed later. The assumption with Equation 2.1.5 dictates the use of a small crystal outside a resonant cavity. In addition, it assumes the beam seen by the crystal is a plane wave with no divergence or change in waist. Note that the SHG process is a major function of length, area, and power. Typically, in CW cases, placing the NLO material inside the fundamental Fabry Perot cavity induces a high enhancement providing the most efficient conversion. A more effective calculation for single pass conversion, including a depleted pump case, which may be present in a cavity, involves

$$P_{2\omega} = P_{\omega} \cdot \tanh^2 \left(L \cdot \sqrt{2 \cdot \eta_o^3 \omega_1^2 \cdot d_{eff}^2} \cdot \left(\frac{P_{\omega}}{\pi \cdot w^2} \right)^{\frac{1}{2}} \right). \quad (2.1.7)$$

η_o is the resistance in free space divided by the index of refraction. Equation 2.1.7 is still a plane wave model. For further modeling details of the SHG interaction process, refer to Ref. [6]. By plotting this equation at parameters matching experimental setups, the result can be mapped into a squared function. Note that when mapped into a squared function, this is similar to Equation 2.1.5. The power of the second harmonic generated light is proportional to the square of the fundamental power.

The polarization describing optical systems where the field present causes a change in the polarization can be written as,

$$P(t) = \chi^{(1)} \cdot E(t) + \chi^{(2)} \cdot (E(t))^2 + \chi^{(3)} \cdot (E(t))^3 \dots \quad (2.1.8)$$

$\chi^{(1)}$ denotes the linear susceptibility, and $\chi^{(2)}, \chi^{(3)}$ denote the second and third order nonlinear susceptibility. The d_{eff} term stems from the $\chi^{(2)}$ term. The relation is as follows,

$$P(t) = 2 \cdot d \cdot E(t)^2. \quad (2.1.9)$$

Note that some authors use d to represent $d \cdot \epsilon_o$. This d term is a coefficient representing the change in a given direction, ie. xx, yy, zz, yz, xz, and xy directions. The d_{eff} term relates to these corresponding d terms through some formula based on

crystal structure. For more information, see Ref. [5]. For example, the d_{eff} expression for beta-barium borate is

$$d_{eff} = d_{31} \cdot \sin(\theta_{P.M.A} + \alpha_{W.O.}) + (d_{11} \cdot \cos(\phi) - d_{22} \cdot \sin(3 \cdot \phi)) \cdot \cos(\theta_{P.M.A} + \alpha_{W.O.}) \quad (2.1.10)$$

$\theta_{P.M.A.}$ the phase matching angle described above. $\alpha_{W.O.}$ is the walk-off angle in the crystal. ϕ is the phi angle at phase matching. d_{31} , d_{11} , and d_{22} are the d terms in the zx, xx, and yy directions previously described. At 1064 nm beta-barium borate has $d_{31} = 1.13 \cdot 10^{-13} \frac{m}{V}$, $d_{11} = 2.3 \cdot 10^{-12} \frac{m}{V}$, and $d_{22} = 1.13 \cdot 10^{-13} \frac{m}{V}$. For beta-barium borate, the phase matching angle is 22.8° , phi angle of 0° , and a walk-off angle of 2.7° . Walk-off angle is the difference between the propagation vector and the Poynting vector. The d_{eff} term is $2.09 \cdot 10^{-12} \frac{m}{V}$.

Another modeling consideration is the beam waist. With a smaller waist, a higher conversion efficiency is expected. The semiconductor industry has been one of the major driving forces behind development of small wavelength lasers. In focusing beams to a small spot size, wavelength plays an important role. Since focusing a laser down requires focusing optics, there is a practical physical focusing limit. The simple expression of the waist focused through a lens using a Gaussian beam states,

$$w_f = \frac{\lambda \cdot f}{\pi \cdot w_i} \quad (2.1.11)$$

The smaller spot sizes will allow higher resolution when cutting, blowing links, or imaging. Since the focused waist size is directly proportional to the wavelength,

reduction of wavelength allows a higher resolution. This is another reason for using deep UV sources for semiconductor lithography.

2.2 Possible NLO Materials

Several different types of nonlinear optical crystals are used today for different nonlinear optical applications. Lithium triborate (LBO), beta-barium borate (BBO), potassium dideuterium phosphate (KD*P) and cesium lithium borate (CLBO) are some of the best-known crystals that are used for second harmonic generation. Others include, but not limited to, potassium titanyl phosphate (KTP), neodymium doped yttrium aluminum garnet (Nd:YAG), and lithium niobate LiNbO_3 . All of these crystals mentioned have some advantages and disadvantages. Table 2.2 shows some of the common characteristics for some of the more common crystals.

Table 2.2. Comparison table of different crystal types.

		KD*P	LBO	BBO	CLBO	IP04
Formula		KD ₂ PO ₄	LiB ₃ O ₅	β -BaB ₂ O ₄	CsLiB ₆ O ₁₀	*****
Crystal Structure		Tetragonal	Orthorhombic	Trigonal	Tetragonal	Trigonal
Space Group		I4{bar}2d	Pna2 ₁	R3c	I42d	R32
Class		4{bar}2m	mm2	3m	4{bar}2m	32
		-Uniaxial	Biaxial	-Uniaxial	-Uniaxial	- Uniaxial
Index of Refraction (532 nm)						
	no	1.507	nx = 1.578 ny = 1.606	1.674	1.498	1.777
	ne	1.468	nz = 1.622	1.556	1.445	1.703
Melting Point (deg. C)		235	834	1095	848	*****
Damage Threshold (GW/cm ²)		3	0.4-0.8	0.2	26	>40
Mohs Hardness		2.5	6	4	4	7
deff at 1064 nm (pm/V)		0.776	0.64	2.09	2.39	*****
Transparency Range (nm)						
	Max	1600	2600	3500	2750	2800
	Min	200	160	190	180	165
SHG Phase Matching Range (nm)						
	Type I					
	Max	1600	2600	3500	2750	
	Min	530	551	409.6	477	
	Type II					
	Max		2150	3500	2750	
	Min		790	525	640	

Material “IP04” in Table 2.2 represents “intellectual property” 04, a proprietary material having protection by the company owning the rights to the material. Some information has been intentionally undisclosed to protect those rights. Discussion of “IP04” throughout this thesis will demonstrate why this material was included in this table.

In order to develop a laser at 202 nm, the crystal must be significantly transparent at the desired fundamental and second harmonic wavelengths. Another consideration is the shape of the plotted Sellmeier curves. The Sellmeier equations describe the index of refraction variation over the spectral wavelength range, detailing the conditions for second harmonic generation through phase matching criteria. The Sellmeier equation exists in two forms. The first form states,

$$n(\lambda)^2 = 1 + \sum_i \frac{B_i \lambda^2}{\lambda^2 - C_i}, \quad (2.2.1)$$

where an alternative simplified form states,

$$n(\lambda)^2 = A + \frac{B}{\lambda^2 - C} - D \cdot \lambda^2. \quad (2.2.2)$$

Unfortunately, no knowledge of the derivation between these two different forms was uncovered when researched. Both forms of the equation describe the spectral behavior of the refractive index of that material. Some manufacturers have a combination of both forms.

Optical intensity damage threshold is another important consideration in material selection. Objectively, having the most amount of second harmonic conversion is the goal. Equations 2.1.5 and 2.1.7 both show that $P_{2\omega}$ depends on the fundamental optical intensity $P_\omega / (\pi \cdot w^2)$. High conversion efficiency requires greater energy density, which may result in crystal degradation. Several manufacturers have laser sources in the deep ultraviolet spectrum. However most of their systems required periodic crystal repositioning, even as often as every eight hours, causing

inconvenience and downtime for operators and customers. Deep UV light contains high energy photons. Photon energy is given by

$$E = h\nu = \frac{h \cdot c}{\lambda} . \quad (2.2.3)$$

Photons in 266 nm light have energies greater than 4.6eV, which can degrade materials. With this amount of photon energy, structural bonds often break causing material darkening, cracking, or even pitting.

2.3 Current Deep UV Sources

KLA-Tencor Corporation is a major manufacturer of semiconductor inspection equipment. With the use of excimer lasers, KLA is able to offer a competitive edge in 193 nm inspection equipment, [7]. Argon fluoride is the excimer gain medium producing lasing at 193 nm. Since excimer lasers require frequent gas refills and fluorine is a dangerous gas, the development of deep UV solid-state lasers is an important research topic.

Nikon Corporation currently offers a 193 nm solid-state laser. However, this laser only produces 30 mW of output power, [8]. The disadvantages to this system include five different crystals that mix, sum, and double the Er-doped fiber laser emission providing a 193 nm source. While claiming to have an automated crystal shifting mechanism to prevent crystal degradation, there is still a finite lifetime on the crystal.

Since the crystals Nikon uses in their laser easily degrade, crystal damage is inevitable. This system is not sold in the United States.

Coherent Corporation produces a “BraggStar” industrial argon fluoride excimer laser. The shortest wavelength solid-state laser Coherent offers is the AVIA at 266 nm, [9]. This system produces a maximum average output power of 3 watts at a 30 kHz rep rate. This system is also a diode pumped system.

Newport offers a gas laser at 245 nm. Their solid-state system also is at 266 nm. The output power of this system is unspecified, [10].

2.4 Solid State Schemes for Deep UV

One can get to 202 nm by using either quadrupling a Ti-sapphire or using a dye laser. Currently, there are no 404 nm lasers or laser diodes with significant amounts of affordable power. Affordability is a reason to use 808 nm laser diodes as the pump source and quadruple this wavelength. In order to achieve deep UV light, some scheme of second harmonic generation or wavelength mixing occurs in the optical system.

While the production of a better ultraviolet light source has great opportunities, the energy from these photons can cause optical damage. To minimize damage to optical

components, it is best to produce the desired UV and have it exit the system with minimal interaction on other optical components. The fewer components the UV light interacts with, the less likely optical components will experience darkening or damaging effects. There are many different schemes for laser cavity development. Looking at the simplest may seem like the most logical first step.

2.4.1 Single Pass

Single pass through a NLO crystal will be the easiest way to produce 202 nm laser light. The fundamental power is focused to the desired waist inside the crystal. The generated UV propagates through and exits the laser system only passing through one lens used for collimation and one harmonic separator to remove the pump power. This by far is the simplest approach in laser system development. Later experiments will demonstrate this technique.

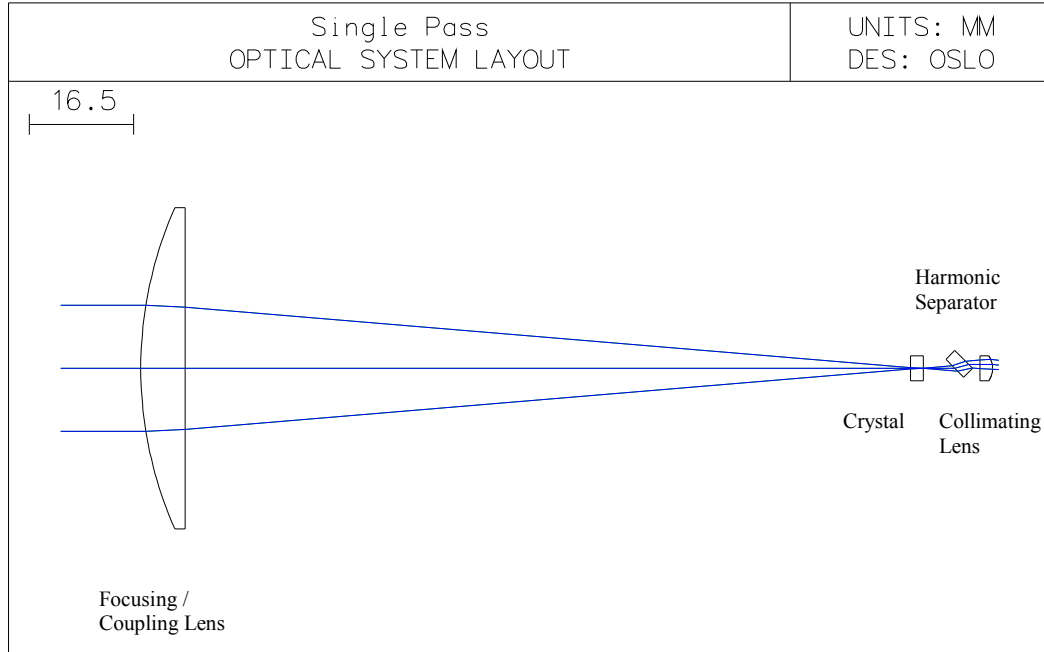


Figure 2.4. Systematic drawing of a lens focused onto a given crystal with beam dump and collimation optics. Lines indicate ray trace through the optical elements using modeling software.

2.4.2 Linear Enhancement Cavity

The next system involves a Fabry Perot design encapsulating the crystal, [11]. This design is simple considering all possible designs, but more complex than single passing through a piece of crystal. This method adds an instability issue of controlling the resonance within the cavity among the list of other engineering problems. Later this paper will explain a control algorithm capable of resolving the instability issue. Once solved, the enhanced internal cavity will allow higher conversion efficiency due to higher energy density.

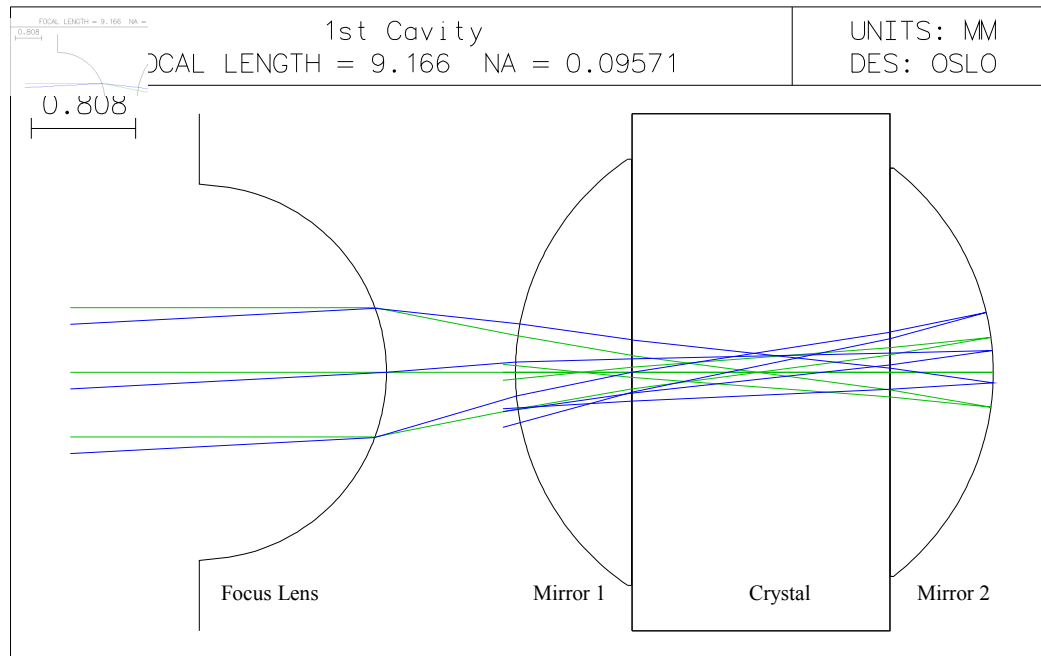


Figure 2.5. Schematic drawing model of a cavity with NLO material. Schematic also show a coupling lens to model mode matching. Orientation of schematic from left to right is, coupling lens, mirror 1, crystal, and mirror2. Cavity also illustrates a cut-away view to show ray trace model inside cavity. Light gray ray trace illustrates a 3° misalignment. The model shows a the beam being reflected back from the second mirror.

Figure 2.5 is an illustration of some modeling performed on an earlier design. The size of the system is rather small and alignment proved to be too difficult. The entire encapsulation of the end mirrors and the crystal is less than 7x7x7 mm. Figure 2.6 shows a more practical application. This Fabry Perot design is much easier to align and implement.

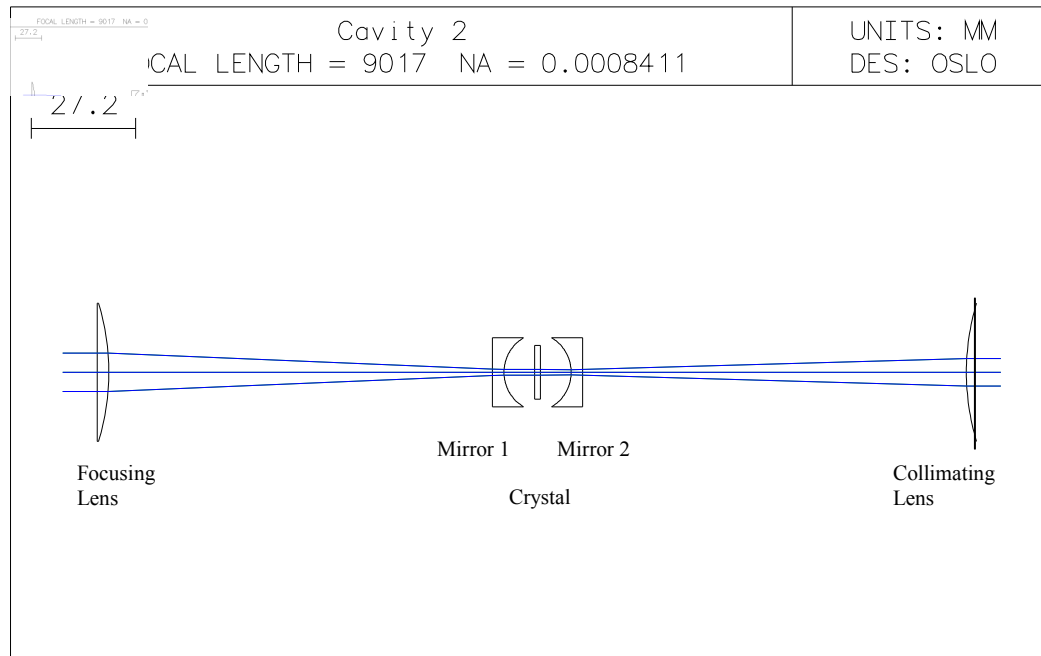


Figure 2.6. Drawing modeling an enhancement cavity for generating 202 nm light. Side view of coupling lens, mirror 1, crystal, mirror 2, and output coupling lens.

By using a two-cavity design and coupling the two stages together with a coupling lens, a laser at a wavelength of 202 nm with an 808 nm seed can come in a nice package. 808 nm diode laser sources are more readily available than laser sources at 404 nm. The disadvantage with using a Fabry Perot setup configuration for both stages is not only the difficulty of alignment, but also the generated UV light also propagates in the reverse direction.

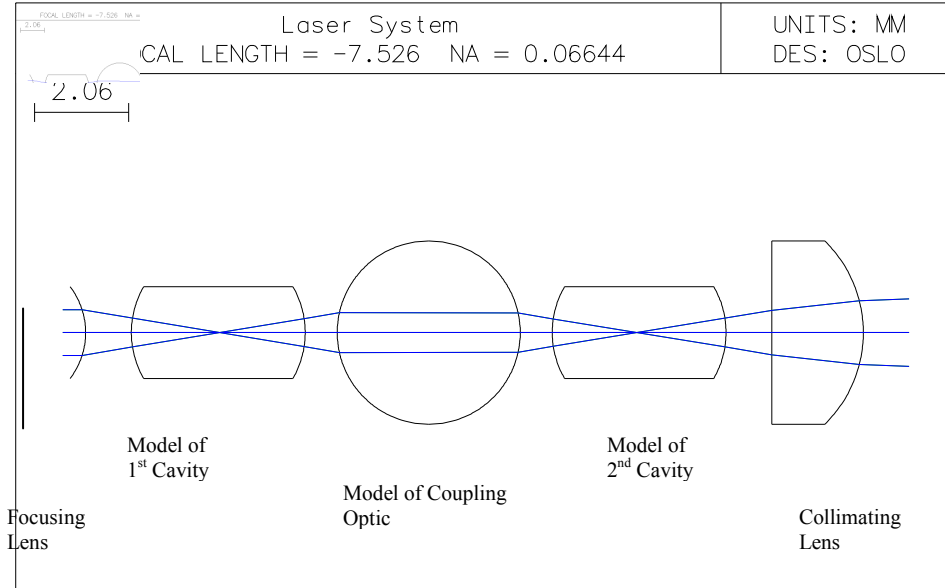


Figure 2.7. Optical schematic model illustrating a two cavity design using an 808 nm seed. Generation of the 404 nm light takes place in the first stage while after a coupling lens 202 nm generation occurs in the second stage. A collimating lens couples the light into a uniform beam. The diagram from left to right indicates a focusing lens, cavity 1, coupling lens, cavity 2, and a collimating lens.

Figure 2.7 is an optical system that complements modeling with the design shown in Figure 2.5. This system uses two cavities to resonate the 808 and 404 nm generating 202 nm. This modeling, done early in the development process, illustrates the possible optical components for the system as a whole. This design provides a systematic flow that implements both stages, only after other major objectives of our design are validated.

2.4.3 Other Cavity Schemes

The “bowtie cavity” is a unique ring cavity design that allows the pump and generated UV signal to propagate only in one (the same) direction, [12]. The

generated UV light will pass through an output coupler in the same fashion as in a linear cavity, just in a single direction reducing or even eliminating UV damage to optical components. Similar to linear cavities the resonating 404 nm provides enhancement thus resulting in a higher energy density. This cavity has another disadvantage. There are more aberrations with the beam because the system has an angular offset in comparison to the linear cavity. Alignment is naturally more difficult due to the added number of optical components.

Optical cavities can be extremely complicated when making the system compact. Several manufacturers reflect the beam back and forth throughout their packaging to make the system compact. Optical cavity design, becoming extremely complicated, requires advanced modeling software. Current software limitations only allow for simplistic designs.

2.4.4 CW/Pulsed

Sections 2.4.1 through 2.4.3 explain simple ways of generating deep UV through explaining different systematical arrangements. These arrangements are useful for both pulsed and constant wave (CW) cases. CW single pass case is straightforward. For multiple pass CW, the average laser power is multiplied by the cavity enhancement, giving circulating power.

For pulsed cases, the peak power in the pulse is significantly greater than the average power, allowing higher conversion efficiency. The average power,

$$P_{average} = E_{pulse} \cdot R_{repetitionrate} , \quad (2.4.1)$$

where E_{pulse} is the energy per pulse expressed in joules, and $R_{repetitionrate}$ expresses the repetition rate in hertz. The peak power

$$P_{peak} = \frac{E_{pulse}}{t_{pulse}} , \quad (2.4.2)$$

where t_{pulse} is the full-width half maximum, FWHM of the pulse width. Choosing a laser system can have different advantages and disadvantages depending on the desired criteria needed.

2.5 IP04

As mentioned earlier, Table 2.1 included a new proprietary material. IP04 is a member of the huntites. Huntites are a classification of the crystal structure based on the first crystal discovered of that structure. IP04 is a recent NLO material, which is grown locally. This material may provide a way to dependable solid-state lasers.

Current developments of ultraviolet laser systems provide reliability difficulties to the end user. Several systems have automated crystal-repositioning mechanisms that move the NLO to an undamaged location every few hours. The solution desired; robust crystals that will experience little damage due to intense energy densities

within the crystal. Considering these facts, the only material shown in the Table 2.2 meeting this criterion is IP04.

Since the optical damage threshold of this material is much higher than current NLO materials, higher energy densities can reside within the crystal thus providing higher conversion efficiency. The crystal does not experience surface damage compared to CLBO and BBO. This allows longer run time and no downtime of the laser for required shifting of the NLO material to a new clear aperture.

IP04 is a non-hygroscopic robust material. Water absorption is a problem with BBO. No extensive testing for ultraviolet darkening or damage has yet been performed on IP04. However, some short performance lifetime runs indicate UV darkening will not be a major concern. The material has undergone significant high power testing and characterization with no darkening. Some knowledge of absorption or transmission spectra exists for IP04. Only experimental performance tests will demonstrate the robustness of this material.

3.0 n_e and n_o Sellmeier Equations

Sellmeier equations can be derived from the data taken by an ellipsometer.

Ellipsometry measurements are useful to determine the index of a given material in an axis of direction. This chapter will further investigate the importance of this measurement and the importance of the Sellmeier equations.

3.1 Experiments

Determining the Sellmeier equations is usually done with a spectral ellipsometer on thin materials. With correct orientation of a thin sample, measurements will result in data giving a close approximation of crystal indices. Ellipsometers function by sending polarized light at different wavelengths onto the sample. Monitoring the polarization changes of the reflected light at different incident angles determines the indices of refraction through a process algorithm. Figure 3.1 illustrates a simple block diagram of an ellipsometer.

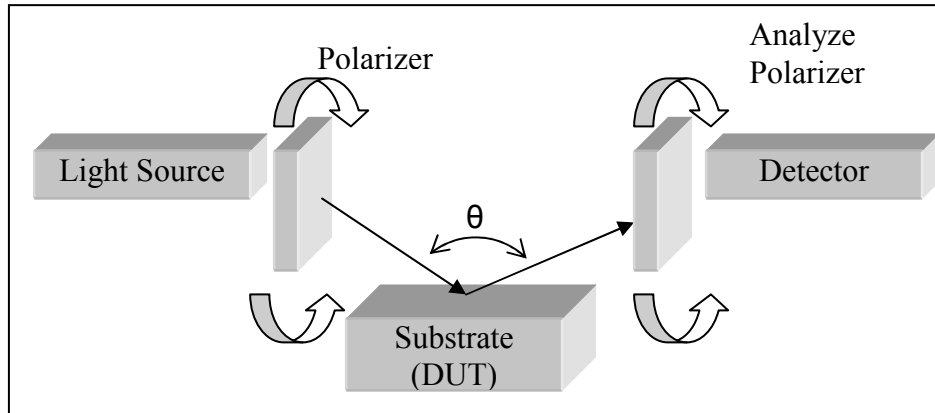


Figure 3.1 Functional diagram of an Ellipsometer. Polarizer and analyzing polarizer rotate for measurements when collecting the data. Theta indicates the angle between the incident and refracted beams.

The estimated Sellmeier equations used for IP04 are plotted in Figure 3.2. However, these curves may not be accurate since there are only four points on these curves from actual phase matching angle data. The points are approximated to fit the Sellmeier equations. Since the Sellmeier equations are estimated, they are subject to error. The exact coefficients will remain confidential at this time to protect intellectual property.

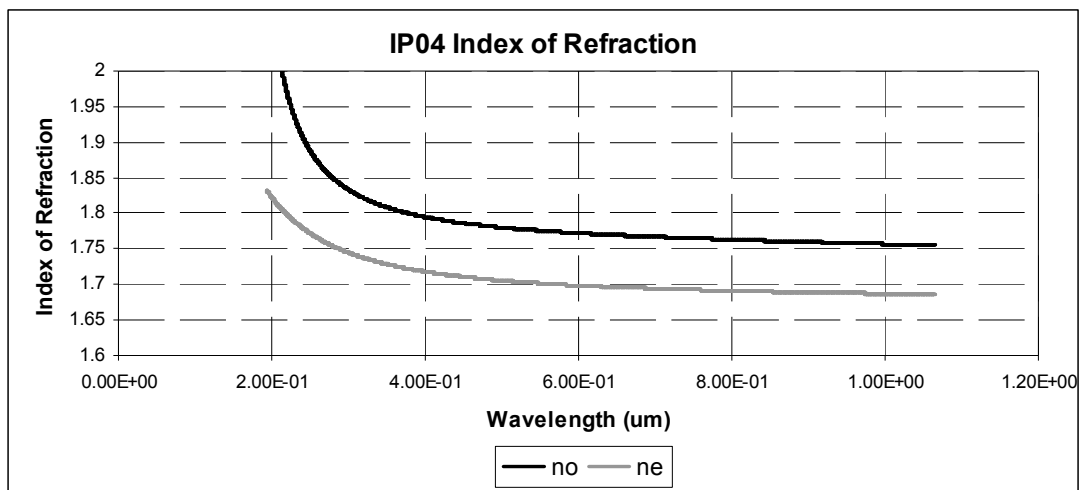
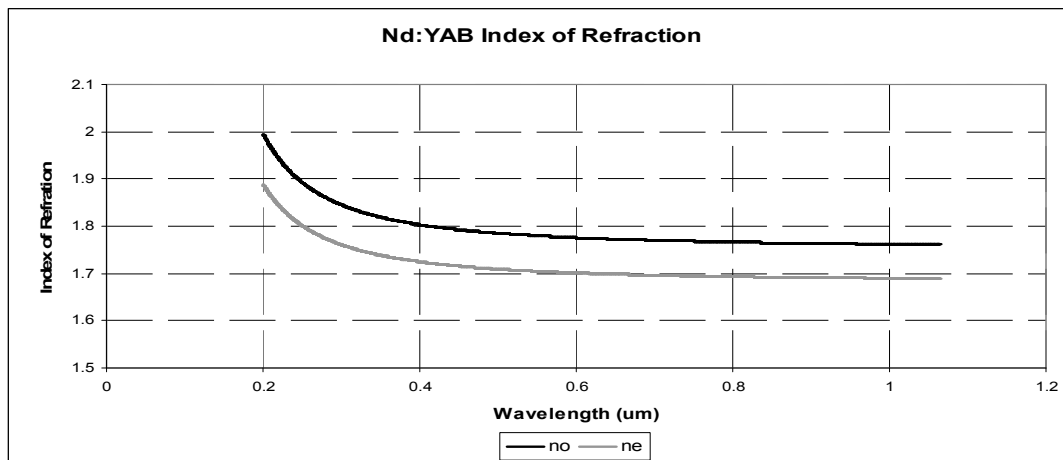
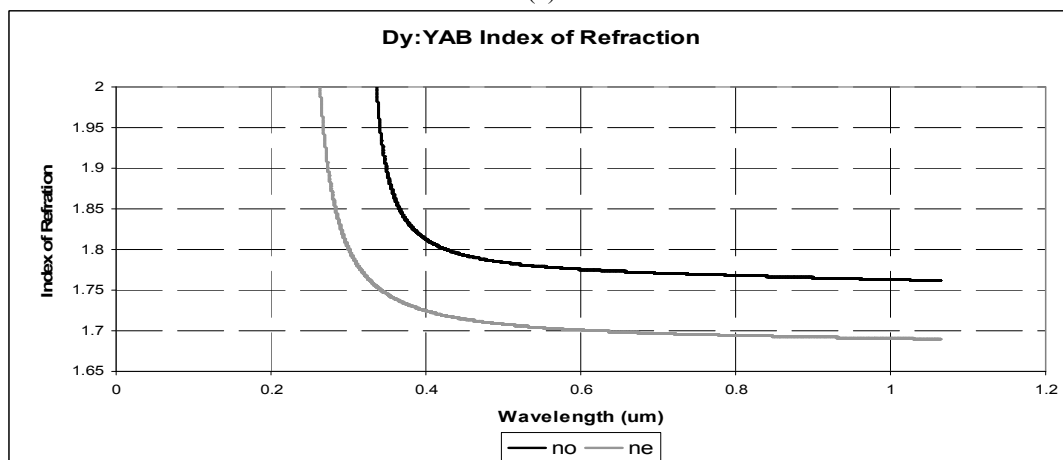


Figure 3.2 IP04 n_e and n_o curves gathered from four measured data points.

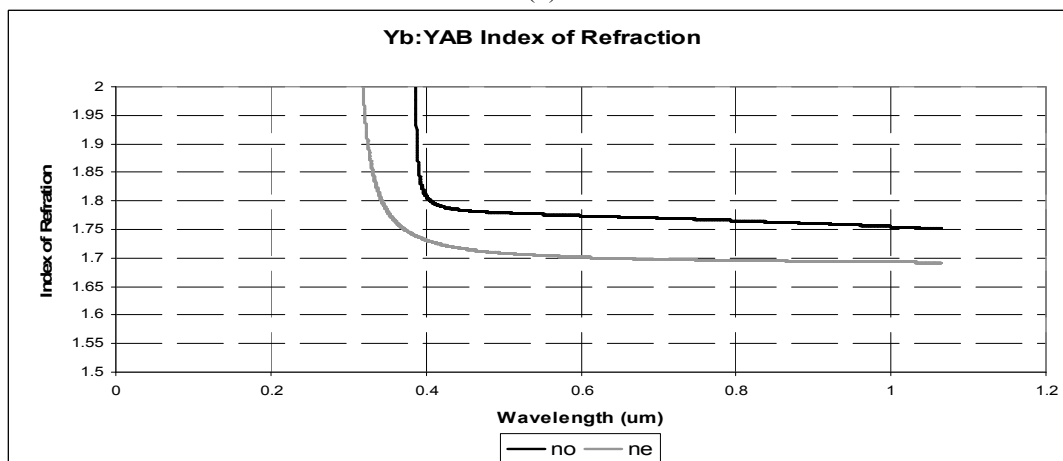
Many different NLO crystals in the huntite family such as Nd:YAB, Dy:YAB, Yd:YAB, and NdSB, have been reported in the literature, [4], [15], [16], [17], [24]. Examining these and other previously mentioned NLO crystals will illustrate the advantages and disadvantages for second harmonic generation. The Sellmeier equations used for n_o , n_e and their coefficients are reported in Appendix A of this thesis. No Sellmeier data is known for NdSB.



(a)



(b)



(c)

Figure 3.3 Indices for different materials. (a) Nd:YAB index of refraction plots graphed from the Sellmeier equations [4] (b) Dy:YAB index of refraction plots graphed from the Sellmeier equations [16] (c) Yb:YAB index of refraction plots graphed from the Sellmeier equations [17].

Figure 3.3 plots the Sellmeier curves for Nd:YAB, Dy:YAB, and Yb:YAB.

Examining these materials demonstrates the possibility of using them as a NLO material for 202 nm generation. Yb:YAB and Dy:YAB have similar Sellmeier plots with absorption tail effects before the desired signal wavelength. Nd:YAB Sellmeier plots reside close together, with no tail effects within the range of interest. Since the maximum phase matching angle is 90 degrees, estimating the phase matching angle close to the maximum will determine if this NLO material is a likely candidate for a direct doubling process at the desired wavelength. The phase matching condition for Nd:YAB at 543 nm occurs at 87.6° . Compared to IP04, these materials do not phase match where IP04 currently can.

There are several different types of crystals produced for different non-linear optical applications. Two common materials that are out on the market for UV applications are Beta-Barium Borate, BBO (BaB_2O_4), and Cesium Lithium Borate, CLBO, ($\text{CsLiB}_6\text{O}_{10}$). These materials are used in lasers frequently for doubling or other nonlinear optical processes, especially in the UV range. Comparing their Sellmeier curves to IP04, one might think that these materials would be likely candidates for an SHG process in the deep UV. However, these crystals have a lower damage threshold limiting the amount of power and, thus, the SHG efficiency. Plots of the Sellmeier equations for these crystals, BBO, and CLBO are shown in Figure 3.4 along with LBO and KD*P for reference.

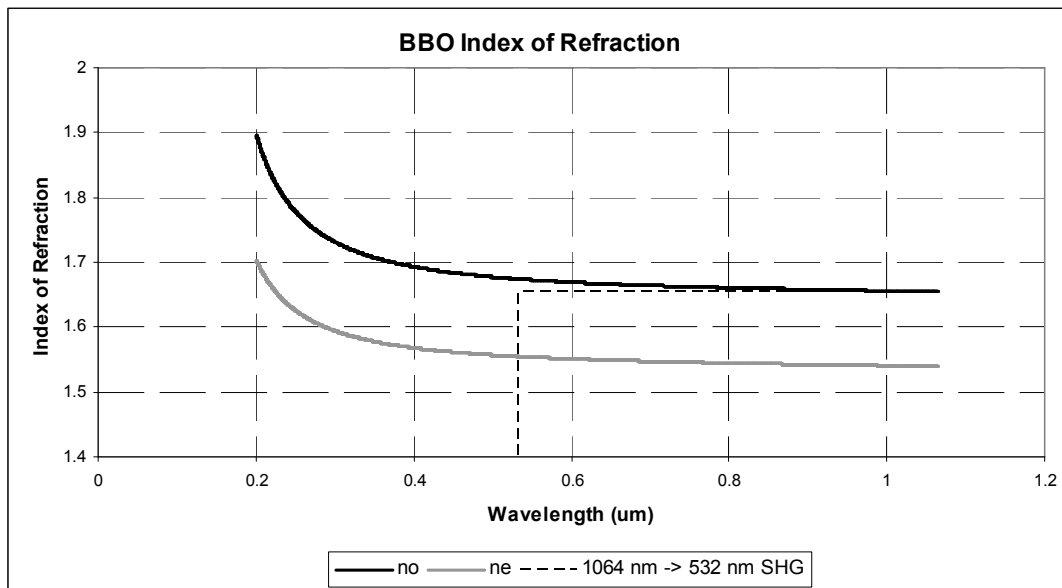


Figure 3.4a BBO index of refraction plots graphed from the Sellmeier equations [22].

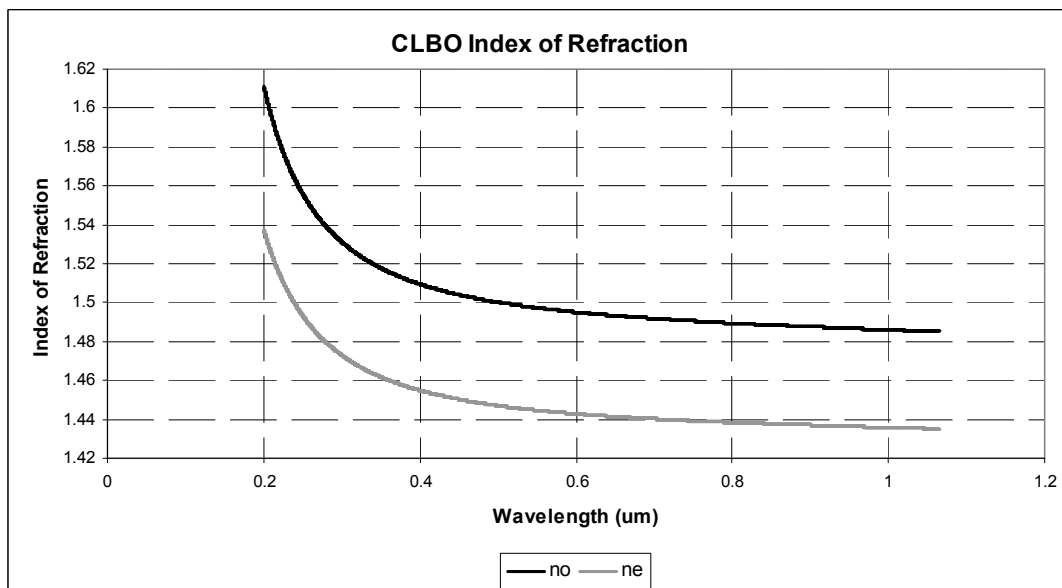


Figure 3.4b CLBO index of refraction plots graphed from the Sellmeier equations [23].

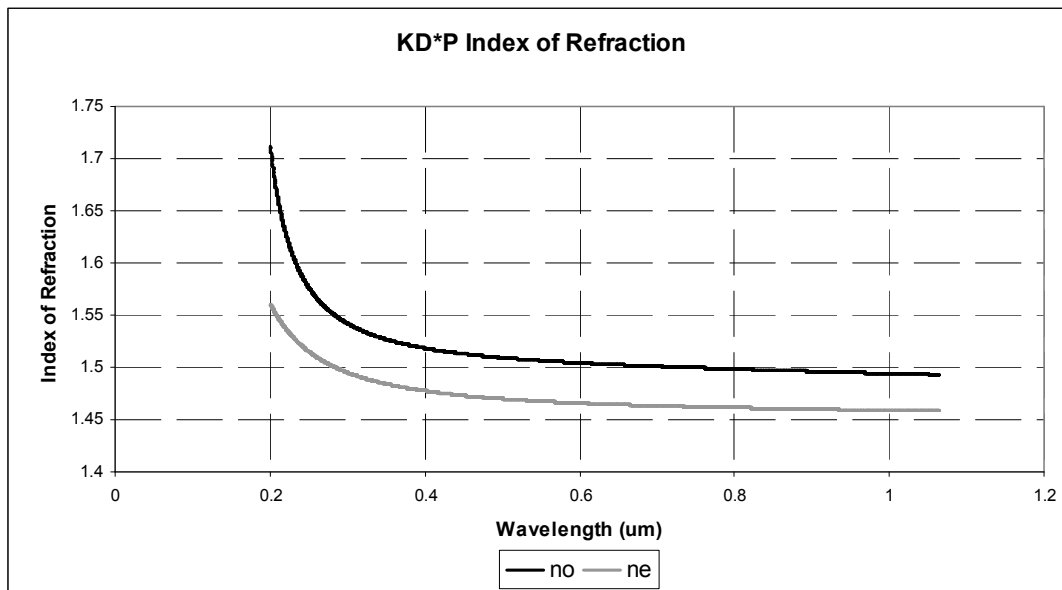


Figure 3.4c KD*P index of refraction plots graphed from the Sellmeier equations [22].

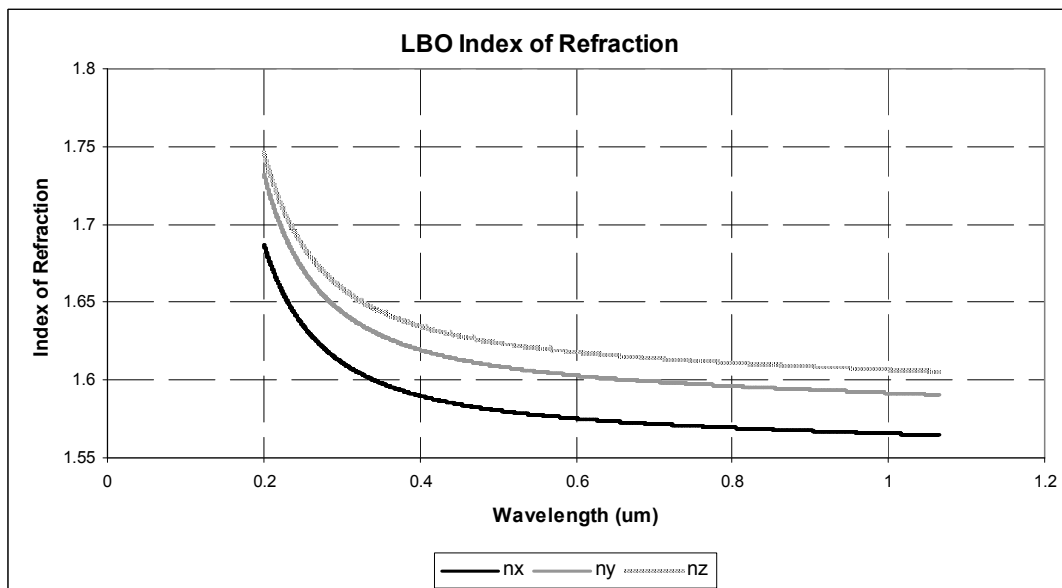


Figure 3.4d LBO index of refraction plots graphed from the Sellmeier equations [22].

Figure 3.4 Sellmeier equation plots for (a) BBO, (b) CLBO, (c) KD*P, and (d) LBO index of refraction curves plotted from the Sellmeier Equations [23],[22].

Continuing the BBO example, in Figure 3.4(a) there is a right angle dashed line drawn on the graph. This indicates the 1064 nm index and the 532 nm location. If

the corner of this right angle is between the n_o and n_e curves (remember BBO is a negative uniaxial crystal), then $n_e(\theta)$ from Equation 2.1.2 can “type-I phase match” with the fundamental index producing the second harmonic. This graphically gives a quick view of a material’s phase matching range.

Using Equation 2.1.3 for a more precise value, CLBO maximum direct doubling occurs at 87.6° producing 235.5 nm, (values are expressed to the nearest nanometer of the fundamental). BBO the other main crystal used to generate UV light phase matches down to 410 nm at 88.7° . Appendix A also contains the Sellmeier equations for these materials and the form used.

IP04 is a promising candidate NLO material since the damage threshold is so high. Visually, Figure 3.2 shows little possibility of phase matching when going to 202 nm from 404 nm. With the estimated Sellmeier equations, and Equations 2.1.2 and 2.1.3, calculations show doubling is not going to be possible. However, frequency summing might be possible for generation of 202 nm. Table 3.1 shows that certain frequency summing combinations can generate 202 nm using IP04. Since no current crystals demonstrate direct doubling at this wavelength, the need for high damage threshold in the crystal is necessary to provide sum-frequency mixing. This process is more inefficient as $d_{\text{effective}}$ decreases due to the increase in phase matching angle.

Table 3.1 Wavelength mixing and phase matching angle chart for IP04. The first portion of the chart shows calculations to generate 202 nm, while the second portion of the chart shows a close wavelength with currently available sources.

Harmonic Order	Fundamental Sum 1 (m)	Fundamental Sum 2 (m)	Signal (m)	Type I Phase Matching Possible?
2	404.E-9	404.E-9	202.E-9	NO
3	606.E-9	303.E-9	202.E-9	NO
4	808.E-9	269.E-9	202.E-9	YES
5	1.01E-6	252.E-9	202.E-9	YES
6	1.212E-6	242.E-9	202.E-9	YES
7	1.414E-6	235.E-9	202.E-9	YES
8	1.616E-6	230.E-9	202.E-9	YES
5	1.06E-06	266.E-09	213.E-09	YES

As one can see from the previous table, getting to 202 nm requires some unique wavelengths. Included in this table is a fifth harmonic of 1064 nm. 1064 nm and 266 nm generates 213 nm; 266 nm is a standard UV source and 1064 nm, ($266 \text{ nm} \cdot 4 = 1064 \text{ nm}$), is a valid pump source. The phase matching angles of IP04 are not included; however, whether the possibility for a given sum-frequency mixing process is listed.

The particular interest in Table 3.1 is the fourth harmonic. Even though direct doubling is not obtainable with our current system, three different crystal orientations for three different sum-frequency combinations can get to 202 nm. Table 3.2 shows the possibilities.

Table 3.2 Wavelength mixing and phase matching chart to achieve 202 nm.

Harmonic Order	Fundamental Sum 1 (m)	Fundamental Sum 2 (m)	Signal (m)	Type I Phase Matching Possible?
2	808.E-9	808.E-9	404.E-9	YES
3	808.E-9	404.E-9	269.E-9	YES
4	808.E-9	269.E-9	202.E-9	YES

Current sources at 193 nm are excimer lasers. Table 3.3 shows the possibility of achieving 193 nm in a solid-state system. Similar to the correlation between Tables 3.1 and 3.2 are Tables 3.3 and 3.4. Table 3.4 also includes a way of producing 193 nm with a 1550 nm source.

Table 3.3 Wavelength mixing and phase matching chart for 193 nm.

Harmonic Order	Fundamental Sum 1 (m)	Fundamental Sum 2 (m)	Signal (m)	Type I Phase Matching Possible?
2	386.E-9	386.E-9	193.E-9	NO
3	579.E-9	289.E-9	193.E-9	NO
4	772.E-9	257.E-9	193.E-9	YES
5	965.E-9	241.E-9	193.E-9	YES
6	1.158E-6	231.E-9	193.E-9	YES
7	1.351E-6	225.E-9	193.E-9	YES
8	1.544E-6	220.E-9	193.E-9	YES

Phase matching for the second and third harmonic are not possible, which is no surprise since the second and third harmonics do not phase match for 202 nm. There is a possibility of frequency mixing.

Table 3.4 Wavelength mixing and phase matching using a 1550 nm source.

Harmonic Order	Fundamental Sum 1 (m)	Fundamental Sum 2 (m)	Signal (m)	Type I Phase Matching Possible?
2	1.55E-6	1.55E-6	775.E-3	YES
3	1.55E-6	775.E-3	516.E-3	YES
4	1.55E-6	516.E-3	387.E-3	YES
5	1.55E-6	387.E-3	310.E-3	YES
6	1.55E-6	310.E-3	258.E-3	YES
7	1.55E-6	258.E-9	221.E-9	YES
8	1.55E-6	221.E-9	193.E-9	YES

All of these phase matching angle possibilities are from the estimated Sellmeier equations. To verify the validity of these equations, one needs to map out the indices of refraction through ellipsometry measurements or try to generate 202 nm light from a 404 nm source. Either of these methods will indicate what happens to the material in the deep UV range.

3.2 Results

Ellipsometry measurements are currently on hold. Ellipsometry measurements will proceed soon when a crystal is grown, cut, and polished with enough window aperture at the required orientation. Using a dye laser, the phase matching angle found for a corresponding wavelength can extrapolate out the index of refraction. This will give one more data point on the Sellmeier curves in the deep UV region. Again, as previously mentioned, either ellipsometry measurements or an SHG process knowing the phase matching conditions will verify the validity of the estimated Sellmeier equations.

4.0 200 nm Experiments

This chapter examines SHG at various phase matching angles. Determining the SHG phase matching criteria will demonstrate the full potential of IP04 as a new NLO material.

4.1 Experiments

The first step to 202 nm was to use a 1064 nm laser. This might sound strange but the crystal used has a known 266 nm second harmonic generation phase matching angle for 1064 nm to 532 nm and 532 nm to 266 nm. The idea is to develop and refine this process for an 808 nm pump rather than a 1064 nm pump.

The idea for verifying 202 nm generation using an 808 nm source is the simplest and cheapest approach. 808 nm sources are easy to obtain and come in convenient laser diode packages. Using a piece of LBO with characterized phase matching angles will help in the first stage of second harmonic conversion. This simplifies the approach.

Previous approximated Sellmeier equations for IP04 predict no 404 nm to 202 nm SHG phase matching possibility. Placing a fractured piece of IP04 crystal (small crystal fragments in the form of a powder could also be used) in front of a 404 nm laser source and finding a refracted 202 nm beam would verify that the approximate

Sellmeier equations are inaccurate. [With greater phase matching probability from IP04 dust, detection of a diffuse SHG signal requires a sensitive spectrometer.] A 404 nm pulsed dye laser is used for the source. A fiber-coupled UV Ocean Optics spectrometer is used to detect the SHG signal. Locating the signal involves trying to capture a particular steradian capable of delivering enough 202 nm light recognizable by the fiber spectrometer. Verifying the spectrum for a narrow laser peak at 202 nm confirms the crystal can achieve second harmonic generation at 202 nm. Using the fractured crystal with the 404 nm source, the likelihood of achieving and viewing phase matching angle is far greater and quicker than to grow, cut, and polish crystals at several different angles.

To additionally validate the estimated Sellmeier equations, the predicted and measured phase matching angles for 235 nm generation can be compared. IP04 material cut at a phase matching angle for 266 nm generation allows some angular tuning, around $\pm 10^\circ$. This tuning range allows use of a 266 nm oriented piece of IP04 for 235 nm SHG testing.

4.2 Results

Two different experiments performed provided substantial evidence relating to the Sellmeier equations. The first experiment examined direct doubling of a 404 nm laser and the second experiment measured the phase matching angle for 235 nm

generation. Also included in this section is a subsection containing information obtained about IP04's temperature bandwidth. Since no information about this material is known, the experiment to perform this measurement occurred as a byproduct.

4.2.1 Second Harmonic Generation from 404 nm

Eventually obtained with a pulsed 404 nm dye laser source, a direct SHG signal is observed around 202 nm. This data shows that the Sellmeier equations are uncertain in the deep UV range. More accurate Sellmeier equations should confirm the possibility of SHG at 202 nm.

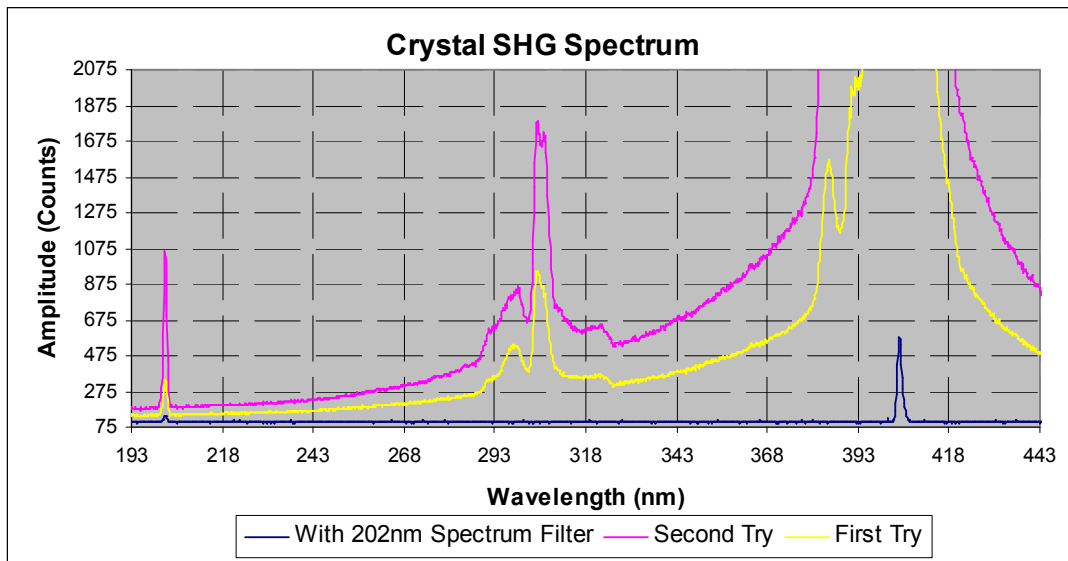


Figure 4.1. 202 nm spectrum data captured with an Ocean Optics Spectrometer. Three different data sets are shown in graph. Last data set taken, first in legend, is with a narrow band, 200 ± 10 nm, 10% transmission filter.

Figure 4.1 demonstrates the possibility of 202 nm generation through direct doubling. Currently no index data points are available at this wavelength. The last data point for the Sellmeier equations is at 266 nm. The amplitude shown in the Figure 4.1 is an arbitrary unit of measure. Since coupling efficiency is difficult to measure for a fiber spectrometer, no power measurements can be deduced from this data. Even with a filter having an estimated 10^3 attenuation at 404 nm, it is still difficult to estimate the amount of 202 nm generated.

In Figure 4.1, there is another feature seen around 300 nm in the non-filtered plot data. The approximate 5000 cm^{-1} shift is too great to be an anti-Stokes Raman shift from the two turning prisms before the crystal. The triple peak is seen even when the crystal is removed from the setup and when the pump laser is directly coupled into the spectrometer without the fiber. The origin of this spurious signal is unknown but is unrelated to the IP04 crystal and the 202 nm peak.

4.2.2 Phase Matching Angles for 235 nm generation

A 470 nm dye laser provides an excellent source for determining the second harmonic 235 nm phase matching angle. The measured internal phase matching angle for 235 nm in IP04 is 11 degrees different from Sellmeier predictions. The direction of angle variation predicts the possibility of deeper UV generation through a direct doubling process in IP04 in support of the 202 nm observation.

4.2.3 Temperature Bandwidth

Measurements of temperature versus second harmonic generation intensity show greater than a 35 °C window for SHG. Data spanning over a 35-degree window centered at room temperature shows SHG variation of only fractions of a percent. When measurements of SHG occurred, a concern was expressed about the possible heating of IP04. Within this 35-degree range, the fluctuations of the SHG output were minimal dismissing heating effects as a concern. This setup was not configured to measure $\delta n / \delta T$ for employment into equation 2.1.4. Further investigation may provide interesting results for the material used.

5.0 Electro-optic Measurements

Using intra-cavity electro-optic modulators as Q-switches might produce a pulsed system with high peak power. This chapter examines the possibility of using IP04 as an electro-optic device.

5.1 Experiments

The setup for this experiment is rather simple. Using a scheme similar to polarization rotators, an analyzer polarizer placed at the end helps determine the output signal.

Figure 5.1 is a detailed drawing of the setup. By applying an electric field across the crystal under test (CUT), the output beam will either pass through, be absorbed by the analyzer polarizer, or some degree in between.

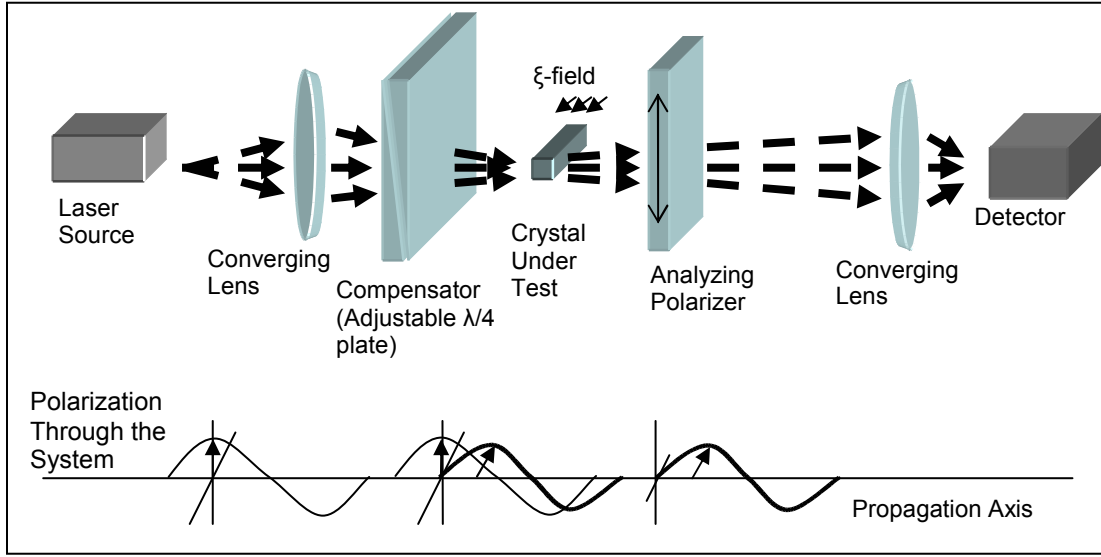


Figure 5.1 Schematic drawing of the setup used for Electro-optic modulation. Polarization information shown in the lower part of this figure illustrates polarization information after the laser, compensation plate and crystal.

Using the matrix expression

$$M_{TR} = \begin{bmatrix} \cos(\theta) \cdot \cos(\phi) + \sin(\theta) \cdot \sin(\xi) \cdot \sin(\phi) & \sin(\theta) \cdot \cos(\xi) & -\cos(\theta) \cdot \sin(\phi) + \sin(\theta) \cdot \sin(\xi) \cdot \cos(\phi) \\ -\sin(\theta) \cdot \cos(\phi) + \cos(\theta) \cdot \sin(\xi) \cdot \sin(\phi) & \cos(\theta) \cdot \cos(\xi) & \sin(\theta) \cdot \sin(\phi) + \cos(\theta) \cdot \sin(\xi) \cdot \cos(\phi) \\ \cos(\xi) \sin(\phi) & -\sin(\xi) & \cos(\xi) \cdot \cos(\phi) \end{bmatrix} \quad (5.1.1)$$

the coordinate transformation allows the index ellipsoid to be represented in a frame similar to the laboratory environment. Since the CUT has a 32 class structure, the matrix of non-vanishing coefficients is

$$M_{dil} = \begin{bmatrix} r_{11} & \cdot & \cdot \\ -r_{11} & \cdot & \cdot \\ \cdot & \cdot & \cdot \\ r_{41} & \cdot & \cdot \\ \cdot & -r_{41} & \cdot \\ \cdot & r_{11} & \cdot \end{bmatrix}. \quad (5.1.2)$$

Interpolating this expression into a functional form of the index results in

$$\frac{x^2}{n_1^2} + \frac{y^2}{n_2^2} + \frac{z^2}{n_3^2} + \frac{2yz}{n_4^2} + \frac{2xz}{n_5^2} + \frac{2xy}{n_6^2} = 1. \quad (5.1.3)$$

Taking matrix Equation 5.1.2 and multiplying it by the electric field results in the following matrix:

$$M = \begin{bmatrix} r_{11} \cdot E_x \\ -r_{11} \cdot E_x \\ 0 \\ r_{41} \cdot E_x \\ -r_{41} \cdot E_y \\ r_{41} \cdot E_y \end{bmatrix}. \quad (5.1.4)$$

Interpolating from Equation 5.1.3 and matrix in Equation 5.1.4 will correspond to the following form

$$\left(\frac{1}{n_o^2} + r_{11} \cdot E_x \right) \cdot x^2 + \left(\frac{1}{n_o^2} - r_{11} \cdot E_x \right) \cdot y^2 + \frac{z^2}{n_e^2} + 2 \cdot r_{41} \cdot E_x \cdot y \cdot z - 2 \cdot r_{41} \cdot E_y \cdot x \cdot z - 2 \cdot r_{11} \cdot E_y \cdot x \cdot y = 1. \quad (5.1.5)$$

The matrix that results is

$$\begin{bmatrix} \left(\frac{1}{n_o^2} \right) + r_{11} \cdot E_x & -2 \cdot r_{11} \cdot E_y & -2 \cdot r_{41} \cdot E_y \\ -2 \cdot r_{11} \cdot E_y & \left(\frac{1}{n_o^2} \right) - r_{11} \cdot E_x & 2 \cdot r_{41} \cdot E_x \\ -2 \cdot r_{41} \cdot E_y & 2 \cdot r_{41} \cdot E_x & \frac{1}{n_e^2} \end{bmatrix}. \quad (5.1.6)$$

The result of taking the eigenvectors of matrix 5.1.6 will give the coefficients to map the index ellipsoid. Applying an electric field in the X or Y direction will result in a shift in the index ellipsoid. Finding a closed form solution is possible, however it is improbable and lengthy. The frame of reference may shift when an electrical field is applied making the solution to an ellipsoid difficult, [18].

By using Equation 5.1.5, inserting known values, and solving for one axis, the estimated index ellipsoid is easier to plot. Using a mathematics tool, such as Maple, comparing the estimated index ellipsoid with and without an applied field will demonstrate the change in index.

Figure 5.2 shows directional cutaways of the estimated index ellipsoid. An electric field applied in the x-direction of the crystal orientation results in an index shift. Showing two different field strengths and the nominal index, graphically viewing the change is easy.

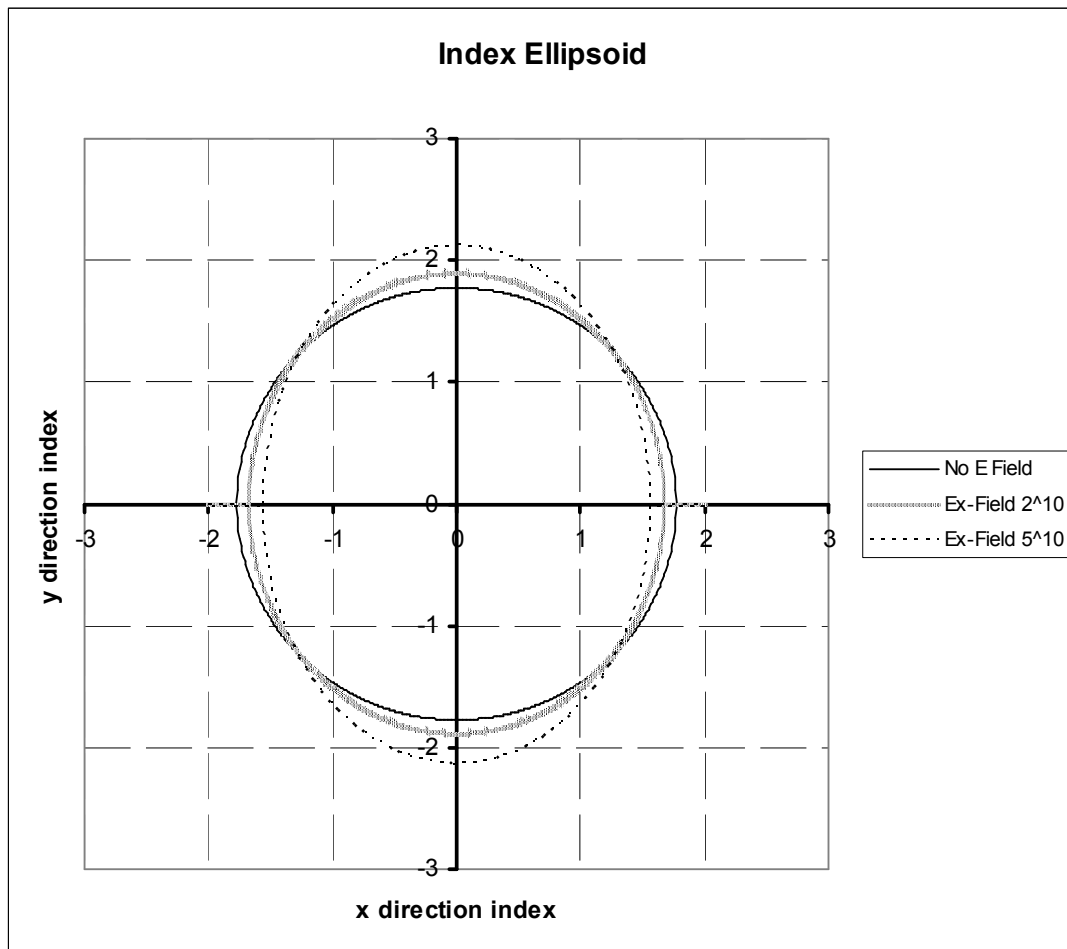


Figure 5.2(a) Index ellipsoid cutaways with E_x field. Cutaway illustrated in the x-y direction. Model of an electric field applied in the x direction at two different field strengths, 2^{10} and 5^{10} . (Exaggerated fields used to help demonstrate index shift.)

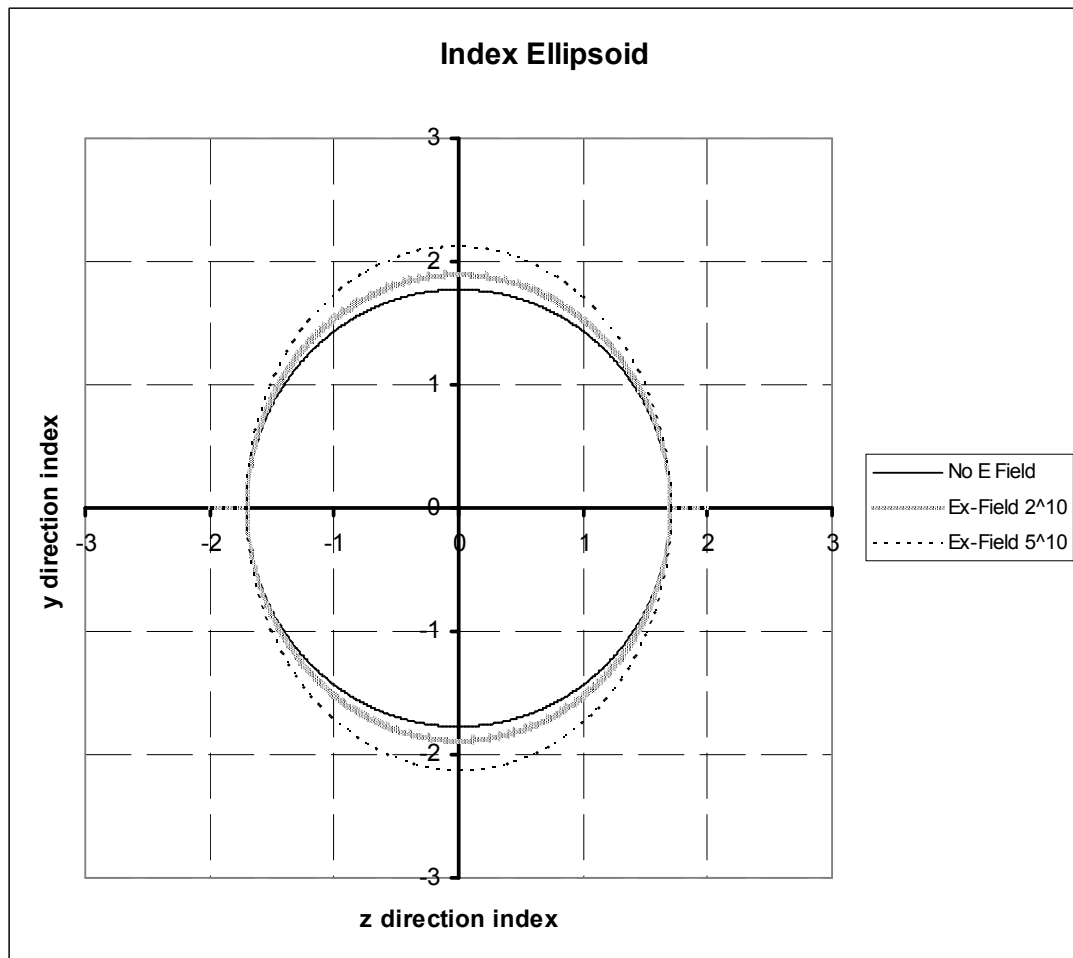


Figure 5.2(b) Index ellipsoid cutaways with Ex field. Cutaway illustrated in the z-y direction. Model of an electric field applied in the x direction at two different field strengths, 2^{10} and 5^{10} . (Exaggerated fields used to help demonstrate index shift.)

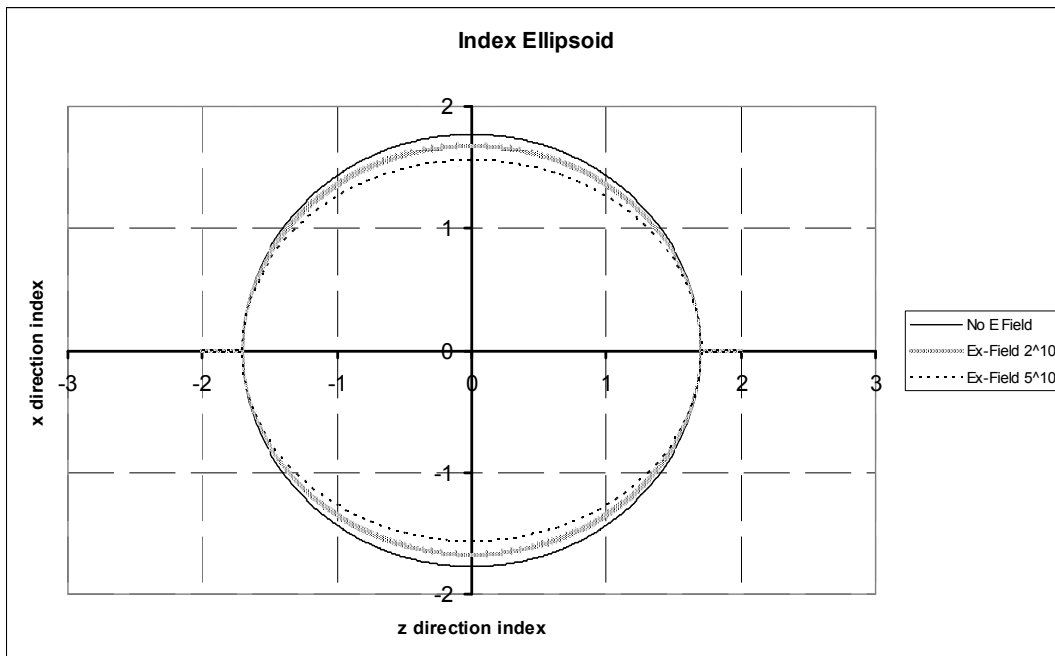


Figure 5.2(c) Index ellipsoid cutaways with E_x field. Cutaway illustrated in the z - x direction. Model of an electric field applied in the x direction at two different field strengths, 2^{10} and 5^{10} . (Exaggerated fields used to help demonstrate index shift.)

Now applying an electric field in the y direction instead of the x direction, the resulting indices shown in Figure 5.3 are cutaways of the estimated index ellipsoid.

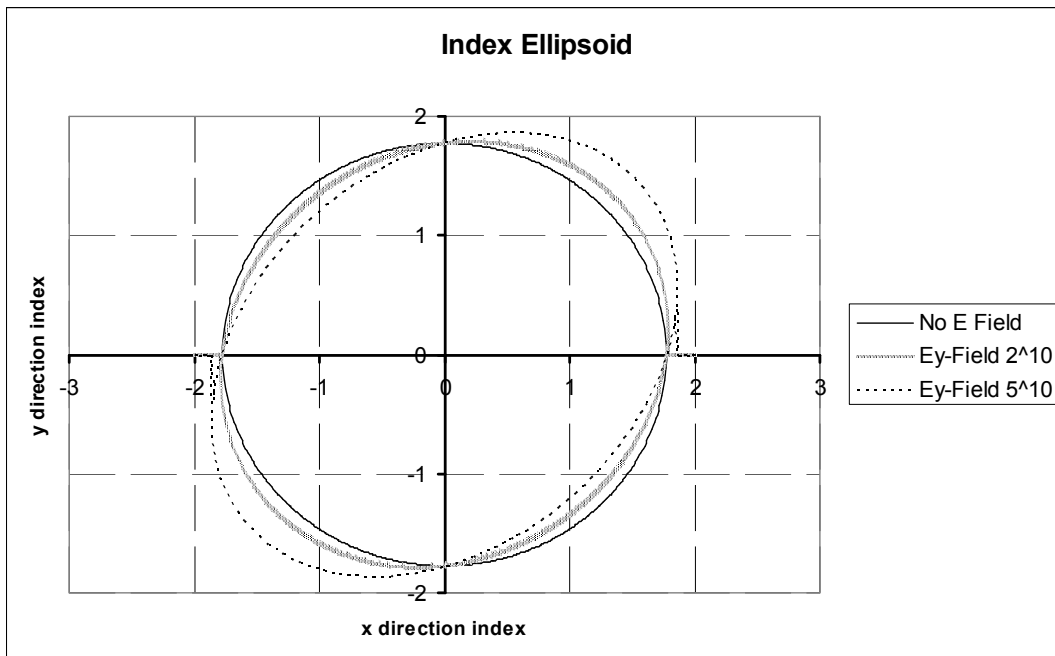


Figure 5.3(a) Index ellipsoid cutaways with E_y field. Cutaway illustrated in the x-y direction. Model of an electric field applied in the y direction at two different field strengths, 2^{10} and 5^{10} . (Exaggerated fields used to help demonstrate index shift.)

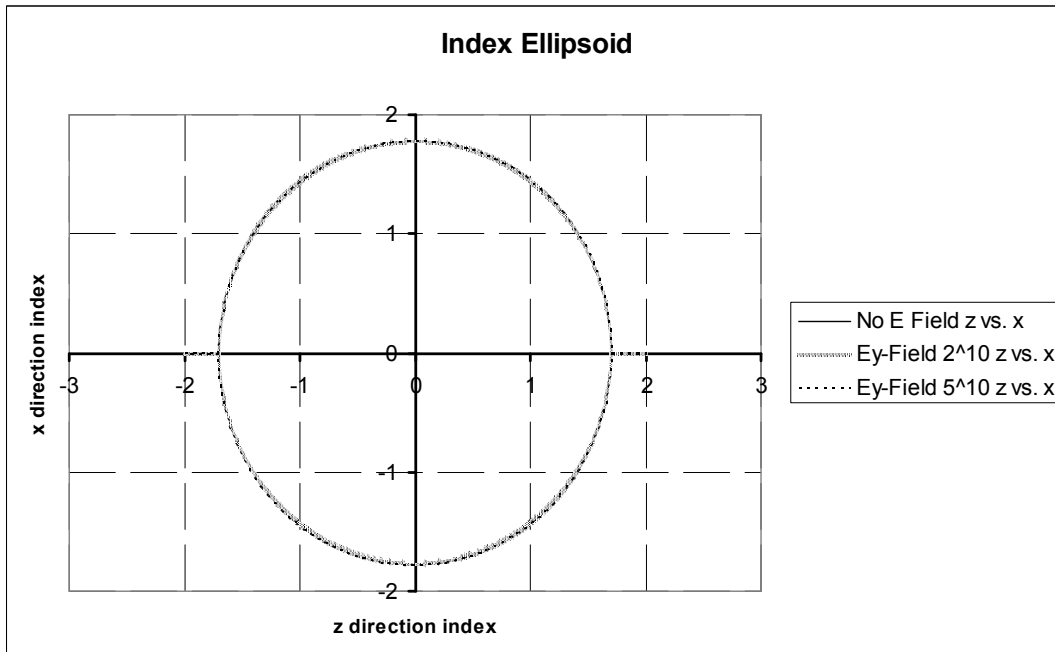


Figure 5.3(b) Index ellipsoid cutaways with E_y field. Cutaway illustrated in the z-x direction. Model of an electric field applied in the y direction at two different field strengths, 2^{10} and 5^{10} . (Exaggerated fields used to help demonstrate index shift.)

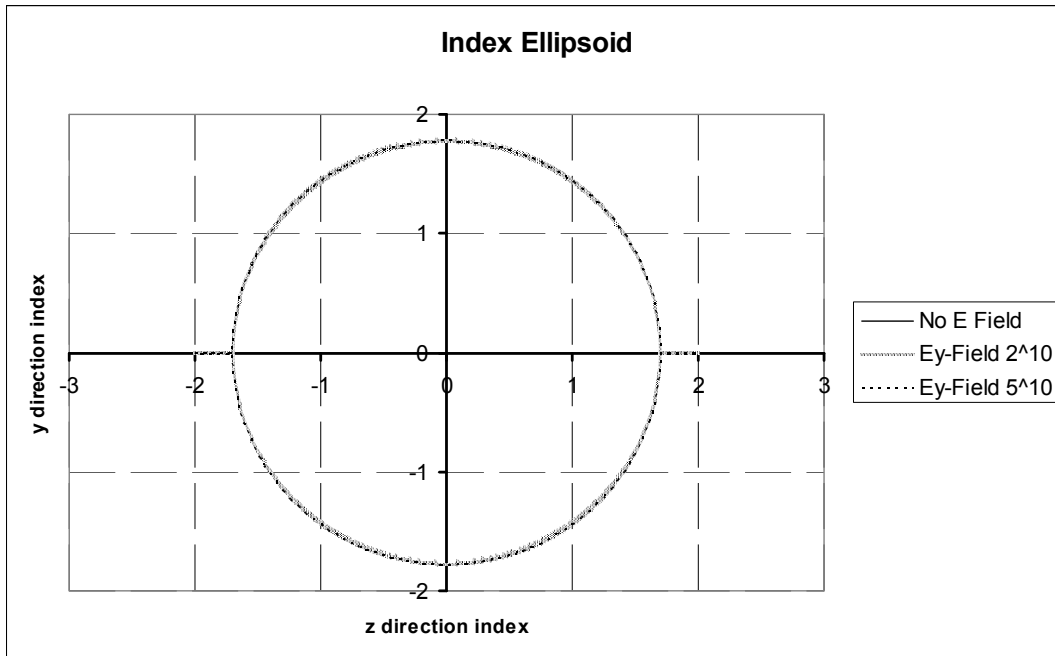


Figure 5.3(c) Index ellipsoid cutaways with E_y field. Cutaway illustrated in the z - y direction. Model of an electric field applied in the y direction at two different field strengths, 2^{10} and 5^{10} . (Exaggerated fields used to help demonstrate index shift.)

Notice that the electric fields modeled to the crystal are massive. This exaggeration helps to understand the movement of the index ellipsoid as an E -field is applied. The dielectric strength is the maximum electric field applied across a given material before it breaks down. The dielectric strength of air is $3 \cdot 10^6 \frac{V}{m}$. Dielectric strengths can vary widely. Teflon, rubber and mylar have dielectric strengths of $60 \cdot 10^6 \frac{V}{m}$, $18 \cdot 10^6 \frac{V}{m}$, and $16 \cdot 10^6 \frac{V}{m}$, respectively. These strengths help give an idea of the maximum applied voltage possible.

After the experiment shown in Figure 5.1 is completed with good results, a more complicated setup will examine the possibility of using a crystal as the NLO material

and a Q-switched medium. Figure 5.4 illustrates the setup for second harmonic generation.

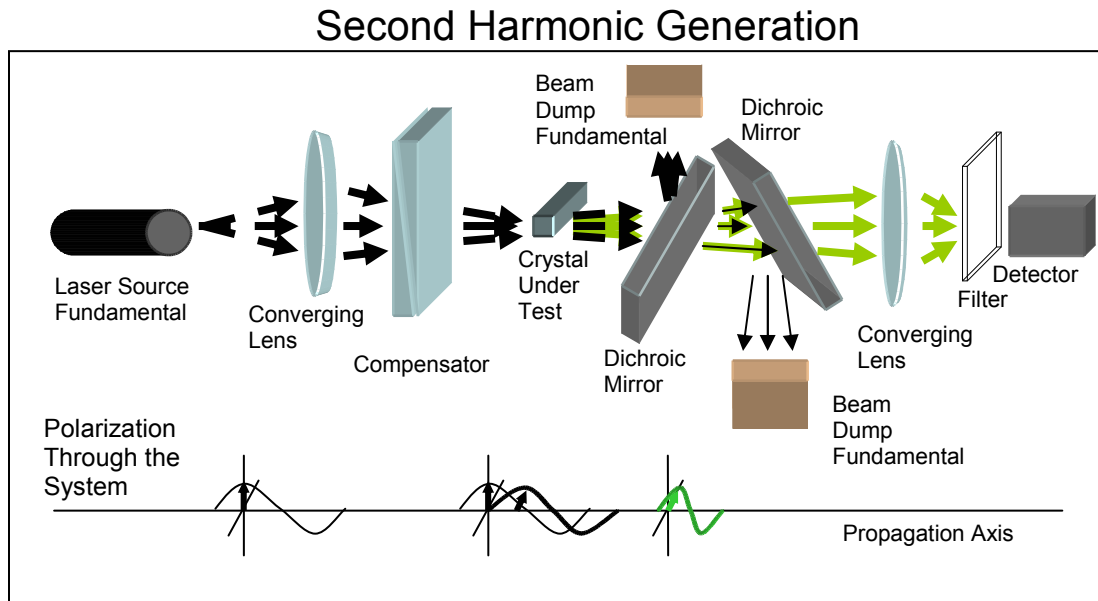


Figure 5.4 Schematic drawing of the setup used to generate the second harmonic. The polarization through the system shows polarization snapshots after the laser, compensator and crystal.

Figure 5.4 does not show the representation of the electric field. The idea is this.

Since the CUT is rotating the polarized light, and SHG involves polarization-dependent light, the combination of these two elements will allow for a Q-switched laser source with one medium. The electric field applied across the crystal will shift the polarization of the beam within the crystal enabling SHG due to index phase matching. Any extraneous fundamental light is dumped before exiting the system.

5.2 Results

Verification of the electro-optic properties by using the NLO as a Q-switched device is unrealistic. Due to the extremely high electric field required across the crystal, the material, behaving like a dielectric, breaks down. Using a piece of crystal approximately 0.5 mm thick and 3000 volts across the crystal, the E-field, $(6 \cdot 10^6 \frac{V}{m})$, was large enough to arc through the crystal and damage the internal structure. This was by far the largest field applied across the crystal resulting in a very small change in polarization. As one can see from Figures 5.2 and 5.3 the electric fields simulated are $20 \frac{GV}{m}$ and $50 \frac{GV}{m}$. These fields are much larger than the breakdown fields of the crystal. These fields were modeled in order to make the small index changes apparent on the figures. The index shift is not large enough to cause a significant change in the propagation of the beam.

Modulation measurements were made after a different piece of crystal was oriented and cut. Applying an electric field along the x crystal axis and rotating the crystal off the z axis, a greater depth of modulation was noted as shown in Figure 5.5. However, only 600 microwatts of modulation was seen. Measurements were made at 0.1 watts unmodulated power at 1064 nm. Since this is not nearly enough modulation, the idea of the using the crystal as a SHG medium and a Q-switched device was no longer pursued.

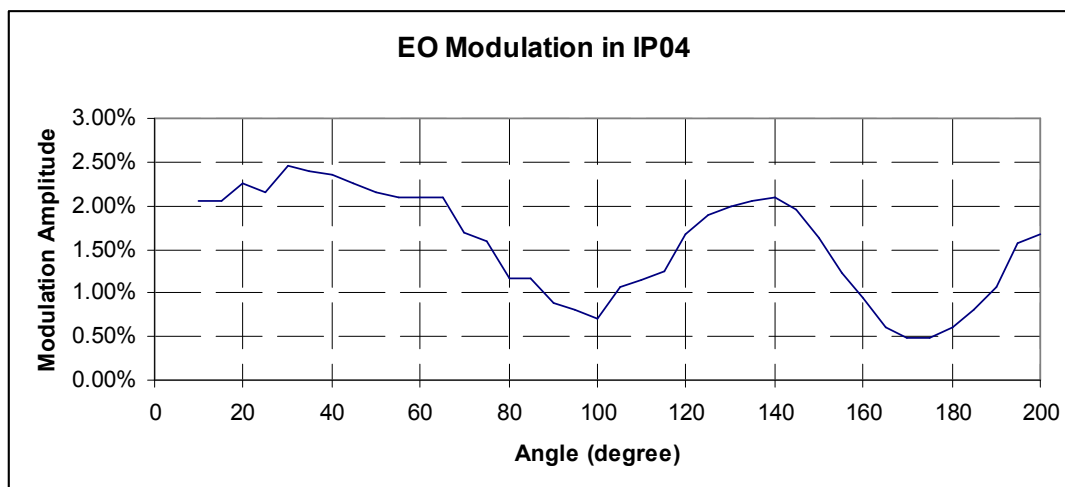


Figure 5.5 Modulation of IP04 verses angle. Field applied in the x direction and rotation about the z axis.

6.0 Cavity Enhancement Control

Resonant cavity enhancement provides greater energy density seen by the crystal compared to a single pass setup. Achieving enhancement involves encapsulating the crystal within an optical cavity. This chapter looks at the optical cavity and examines the controls needed to provide an intensity enhancement seen by the crystal. The main cavity modeled and tested is similar to that previously shown in Figure 2.4. This is important in CW systems to help provide better conversion efficiency.

6.1 Experiments

To generate more 202 nm continuous wave (CW) laser light, a controlled cavity will enhance the energy density seen within the crystal. The structure of a cavity in simple form consists of two end mirrors (one input and one output coupler) and a piezoelectric module moving one of the mirrors to accurately control the length of the cavity allowing light to resonate between these mirrors at an enhanced intensity.

Enhancement of a cavity is described by

$$E = \left(\frac{(1 - R_1) \cdot T_+}{(1 - \sqrt{R_1 \cdot R_2 \cdot T_+ \cdot T_-})} \right)^2. \quad (3.4.1)$$

T_+ is the optical power transmission through the cavity in the forward direction. If an ideal NLO crystal is inside the cavity, the cavity T_+ is set to one. The circulating power inside the cavity on resonance is E from Equation 3.4.1 multiplied by the input

power. The enhancement expression shown in Equation 3.4.1 may look similar to the finesse. Finesse is an arbitrary number that describes the “quality factor” of the cavity. The expression for the finesse is,

$$F = \frac{\pi(R_1 \cdot R_2 \cdot T_+ \cdot T_-)^{\frac{1}{4}}}{1 - \sqrt{R_1 \cdot R_2 \cdot T_+ \cdot T_-}}. \quad (3.4.2)$$

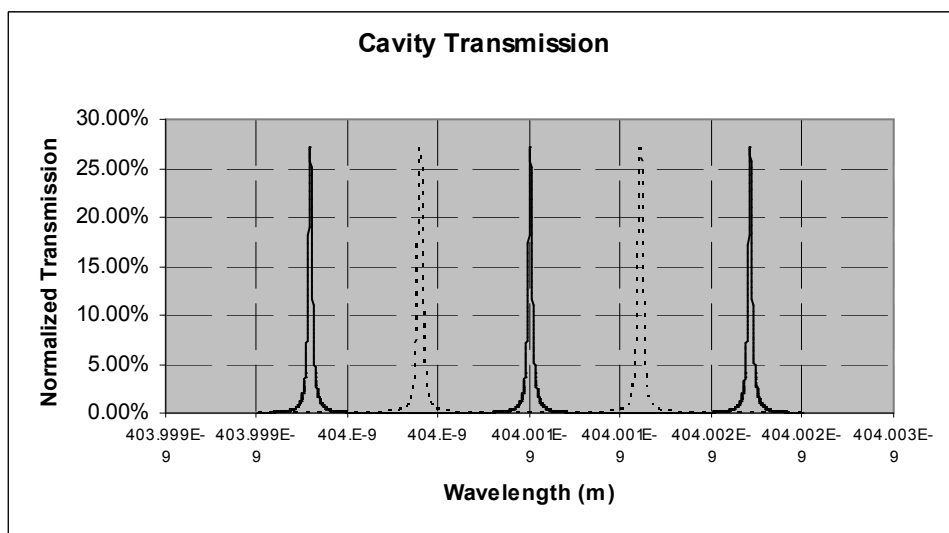


Figure 6.1. Transmission spectrum of a cavity with a length of 45 mm, mirror one at 95% reflectance and mirror two at 98% reflectance. The dashed lines illustrate the cavity length plus $\frac{\lambda}{2}$.

Cavity resonances occur every half wavelength ($\frac{\lambda}{2}$) of cavity length change.

Providing an active feedback using a microcontroller to control the length of the cavity will hold the transmission on a peak (“resonance lock”). This will allow an enhanced cavity to produce more 202 nm light than without active control. Figure 6.1 illustrates the cavity modes separated by the free spectral range (FSR) described as

$$FSR = \frac{c}{2 \cdot n \cdot L}. \quad (3.4.2)$$

Modulating the length of the cavity about the peak with a small signal on the piezoelectric element and detecting the throughput of the cavity provides information to locate the maxima for the feed-forward set point. Performing this feedback feed-forward signal at a high rate and small amplitude allows for a stable enhanced cavity when sampling the feedback signal. Pushing the performance of the feedback feed-forward signal operation permits a dither of the SHG signal that is within the tolerance of the user.

The crucial part in cavity development, with the purpose of achieving high enhancement, involves alignment and mode matching the signal to the cavity mode with coupling optics (lens). Mode matching to the cavity mode has the capability of coupling into higher or lower order transverse modes depending on the quality and accuracy of the focusing scheme. Matching the phase front (radius of curvature of the wave) from a collimated laser beam to the cavity achieves accurate coupling. The cavity will support other transverse modes if coupling is not optimum. Most laser systems take advantage of TEM_{00} mode. This is the fundamental Gaussian spot. Accurate coupling into this mode requires a maximum intensity output compared to other modes. Scanning through at least one FSR for the cavity and comparing the area under the fundamental resonant peak to the area under all other resonant modes gives the coupling efficiency.

For an example of finesse and enhancement, the following cavity is modeled in reference to Figure 6.1.

- $R_1 = 95\%$, radius of curvature = 50 mm
- $R_2 = 98\%$, radius of curvature = 50 mm
- Length = 45 mm
- $T_+ = T_- = 0.975$
- Finesse = 51.43
- Enhancement = 13.89

This list demonstrates the expected enhancement the modeled cavity will generate.

By multiplying the input power, pre-cavity, to the enhancement, a model of the power seen by the crystal can predict the amount of second harmonic optical power expected from the current configuration. If a 10-watt CW laser at a fundamental wavelength were coupled into this modeled cavity, the circulating fundamental power would be 138.9 watts.

6.2 Results

All cavity development in this section uses 532 nm as the fundamental wavelength.

Materials including cavity mirrors and IP04 crystal to build a 404 nm fundamental wavelength resonant cavity were unavailable. The applications between enhancement cavity systems are essentially the same principle regardless of fundamental wavelength.

Cavity stabilization using a digital system provided positive results. Using a 1 kHz sinusoidal waveform enables a half-wave analyzing and updating algorithm. At a 0.5 kHz update rate to a piezoelectric transducer mounted on mirror two, controlling the cavity resonance through cavity length, provided less than 7 percent modulation depth of the signal. The enhanced cavity, remains in resonance while being perturbed by other outside influences. The resonant cavity used in this experiment is not the cavity earlier modeled. The information for this cavity remains as intellectual property.

Shielding from noise is important in order to stabilize the cavity. Using shielded wire helps in the reduction of noise. Noise reduction allows the length of the cavity to remain at the desired set point with little noise amplification on the detected feedback signal.

Several other techniques were discovered since the beginning of the algorithm development process. Some other control methods include the proportional-integral-derivative, Pound-Drever-Hall and Hansch-Couillaud [19], [20]. Some of these methods were implemented and comments comparing these methods might be beneficial for future use; however, if further information is needed, refer to the sources listed.

Pound-Drever-Hall is difficult to implement in our system; therefore, no implementation of this method was performed. By viewing the difference of the

sidebands beat frequencies generated from a modulated phase shift on the fundamental wavelength signal, an active feedback can control an actuator allowing resonance lock. The error function enables an accurate control of the cavity.

Another method published by Hansch Couillaud, [20], involves a polarization element internal to the cavity. Viewing the difference between the back-reflected polarized beams enables a unique error function to actively control the cavity with no consequence to the enhancement dependencies. Implementation of this method is quick and simple. It proved to be very useful in high finesse cavities. Since high finesse cavities require a high “finesse-to-noise ratio”, the error signal provided by this method has a linearized signal between the full-width half maximum of the enhanced peak. The error signal also widens the tails. This makes it easier to retain resonance lock.

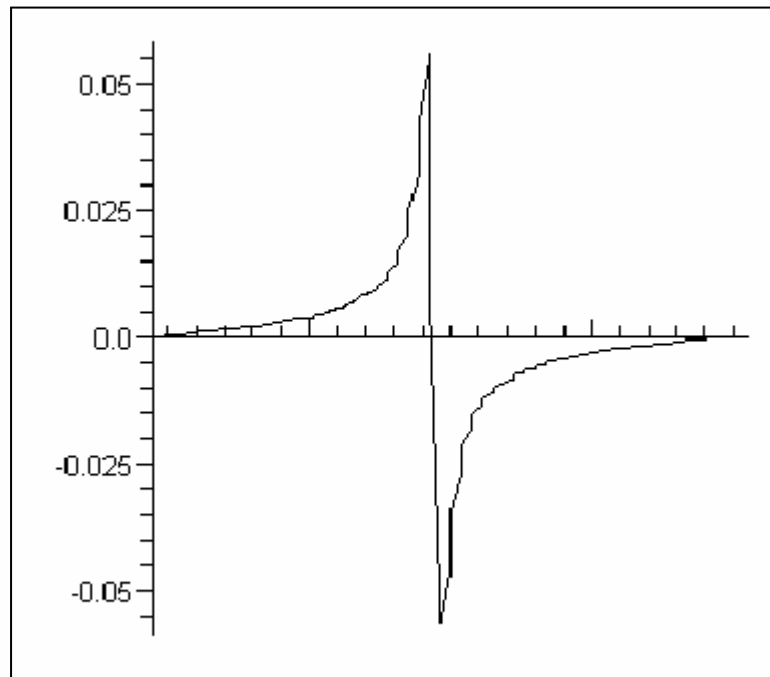


Figure 6.2. Error signal generated for a cavity with a length of 45mm. Plot shows amplitude vs. length error signal for the modeled cavity. Finesse of this cavity is around 51. Horizontal scale is 16 pm. Vertical scale is in arbitrary units.

Figure 6.2 illustrates the error signal modeled. The zero point of the error signal indicates the resonance of the cavity. The convenience is that this error signal offers directional dependence. Figure 6.1 has no directional dependence.

Another control scheme, proportional-integral-derivative (PID), is also successful in obtaining the resonate peak. As long as the set point updates automatically to the maximum feedback signal, resonance lock will occur. The PID approach sets the system output to a given value. The feedback value is either greater or smaller than the set value. For locking a cavity this is not the case. On either side of resonance,

resonance being the set point, the feedback value is less than the set point.

Developing a sign switcher will allow the signal to remain on the resonant peak.

Table 6.1 Truth table of a sign switcher with a positive error signal.

	A(NOT)	A
B(NOT)	+	-
B	-	+

Table 6.1 is a truth table of the sign switcher required to maintain lock at resonance.

“A” is equal to a positive change in the error signal where “A(not)” is a change less than zero. “B” equals the change in the voltage where “B” being greater than zero and “B(not)” less than zero. Table 6.1 reduces to an EXOR not. However, the simulated system has a negative error signal requiring an EXOR. This provides higher cavity stability in contrast to modulating and updating the cavity median.

By implementing the PID control algorithm and the HC method described above, a combination of methods provides a superior locking method. The combination of these two methods eliminates the need for a sign switcher and allows the use of a digital processor for locking. This has an advantage of easy adjustability when implemented into a laser system. Since optically no two systems are exactly the same, digital systems have superior adaptability. The HC method has the advantage of quick error-signal response time. With these two implementations, the modulation and stability on laser systems provides a rigorous solution. High finesse resonant cavities prove to be more difficult to lock. There is a narrowing of the resonance peak and less pronounced lag in the tails of the enhancement and error function

signals. The implementation of these combined methods allows the stabilization of a high finesse cavity and minimal dither in the signal. This method allows for a quicker recovery time if complete resonance lock is broken.

7.0 CONCLUSION

In this thesis, several topics were presented and discussed. The main theme of this thesis was to present a pathway of obtaining a deep UV solid-state laser for use and benefit in industrial applications.

7.1 Recap

The work presented in this thesis included several different experiments.

Ellipsometry measurements were not executed since no IP04 material could be sacrificed for the particular required crystal orientation. Ellipsometry systems are also expensive devices and have limited availability.

202 nm measurements illustrate the need for a well cut crystal at a large theta angles from the c-axis. Shown in SHG measurements using a dye laser, the current Sellmeier equations do not accurately predict the crystal characteristics of IP04 in the deep UV range. Since 202 nm light was generated, detected, and captured, this suggests the possibility of direct doubling process. The 235 nm phase matching angle was also 11 degrees less than previous predictions. These two measurement data points are informative and important in showing the inaccuracies in estimated Sellmeier equations in the UV range.

Electro-optic modulation measurements performed on the IP04 crystal under test show very small effects making this material an improbable Q-switch candidate. Minimal modulation is the result of a small effective electro-optic coefficient.

Cavity enhancement illustrates the use of an analog and digital system for stabilization in a CW scheme. Different control methods presented can be used for particular applications depending on the given system requirements. The current cavity system had an environment with minimal vibration insulation that provided accurate peak tracking with minor fluctuations.

7.2 Future Work

Recommendations for anyone continuing this work involve the following three priority items. First, have a high quality, oriented, and sized piece of IP04 crystal sent out for index mapping of both ordinary and extra-ordinary indices. Second, use the new Sellmeier equations to calculate the type I phase matching angles for SHG process at 235 nm and 202 nm and verify these angles by oriented crystal measurements. Lastly, perform a summing technique to gain confidence in the crystal material characteristics.

Implementing the following ideas may provide more possible uses of the NLO material. Building a laser system with IP04 as the intra cavity NLO material is the

next logical development step. Verification of the 202 nm laser source single pass has been verified. Using a resonant cavity will allow a buildup of 404 nm light giving a gain enhancement that can be developed into a powerful CW laser source.

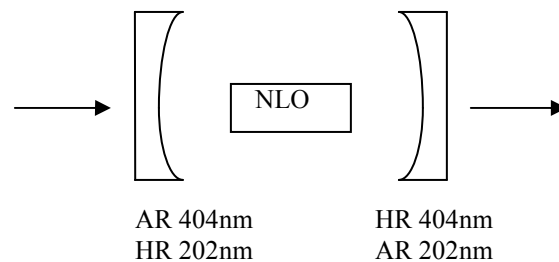


Figure 7.1 Cavity illustrations with coating specifications for laser mirrors.

Since the crystal may have the possibility of laser emission down to 193 nm, development of this new technology would eliminate the problems and hazards of current excimer lasers. This crystal technology will improve current deep UV wavelengths emissions by providing reliable deep UV sources. The suggestion of further investigation of using this material as an NLO at 193 nm only seems logical.

Further investigation into the lower limit of this crystal will provide several lasing wavelength opportunities. The development might provide the opportunity for a deep UV OPO (Optical Parametric Oscillator) or tunable laser. This would be a great device for research applications and may also prove to be a great industrial tool.

Another recommended investigation topic would require considerably amounts of IP04 material. Investigating the exact damage threshold would provide information

on the maximum pump power one could use as a source. Although a lot of material was destroyed in our experiments, the exact damage threshold is uncertain. The crystal surface quality is an important factor in some of the damage that occurred when performing measurements.

Other work would involve the emission and absorption spectra of the IP04 material. When the material was intra-cavity, it was noticed that a red light emitted as a glow from the crystal where the beam propagated. The crystal was in a 532 nm cavity. The possibility of using this material as a gain medium may provide a more effective “red” source. This may prove more difficult than one might think. It might uncover an issue in the growth of the material.

Lastly, investigation of material consistency is important. Although this is more of a growth and development topic, the use of this material in an industrial environment would require such consistency. Throughout our experiments, different crystals had different levels of quality. This may cause some data points to improve as quality improves. Electro-optic measurements, performed early in this project, may also improve with crystal quality because crystal quality has improved throughout this venture.

Bibliography

- [1] Anderson Lee, Claire Liang; Technology Report: Semiconductor, PC, Aerospace, Parker Center for Investment Research, Cornell University, Johnson Graduate School of Management, Sep. 28, 2000
- [2] Photonics.com. Laurin Publishing. 1996-2006. 26 June 2006
<<http://www.photonics.com/directory//dictionary/lookup.asp?url=lookup&entrynum=4717&letter=s>>
- [3] Christopher C. Davis, Lasers and Electro-Optics Fundamentals and Engineering, Cambridge University Press, 1996
- [4] D.Jaque, J. Capmany, F. Molero, and J. Garcia Sole; Blue-light source by sum-frequency mixing in Nd:YAl₃(BO₃)₄; Applied Physics Letters; Vol. 73; pp 3659-3661; 21 December 1998.
- [5] Robert W. Boyd, Nonlinear Optics, 2ed, Academic Press, 2003
- [6] G. D. Boyd, D. A. Kleinman; Parametric Interaction of Focused Gaussian Light Beams, Journal of Applied Physics, Vol. 39, # 8, July 1968
- [7] KLA-Tencor Corporation, <http://www.kla-tencor.com/>, 2005-2007
- [8] 193 nm Solid-State Laser, Nikon, Preliminary, October 2004.
- [9] Coherent, Inc. <http://www.coherent.com/>, 2005-2007
- [10] Newport Corporation & Spectra-Physics, <http://www.newport.com/>, 2006
- [11] M. Rakhmanov, R. L. Savage Jr., D. H. Reitze, D. B. Tanner; Dynamic resonance of light in Fabry-Perot cavities, Physics Letters A, Vol. 305, pp 239-244, 2002
- [12] J. Mes, R. Zinkstok, S. Witte, E.J. v. Duijn, and W. Hogervost; Third harmonic generation of a cw laser in external enhanced cavities, IEEE Symposium, LEOS Benelux Chapter, 2002.
- [13] D. Jaque, J. Capmany, Z. D. Luo and J. Garcia Sole; Optical bands of and energy levels of Nd³⁺ ion in the YAl₃(BO₃)₄ nonlinear laser crystal; Journal of Physics: Condensed Matter; Vol. 9; 1997; pp 9715-9729.

- [14] Hisashi Yoshida, Kazuhiro Fujikawa, Hiroaki Toyoshima, Shinta Watanabe, and Kazuyoshi Ogasawara; Luminescence properties of $\text{YAl}_3(\text{BO}_3)_4$ substituted with Sc^{3+} ions, Physics Statistics Solutions, Vol. 203, No. 11, pp 2701-2704, 2006.
- [15] Peter Dekker, and Judith M. Dawes; Characterization of nonlinear conversion and crystal quality in Nd- and Yd-doped YAB, Optics Express, Vol. 12, No. 24, 29 November 2004.
- [16] R. M. Vazquez, R. Osellame, M. Marangoni, R. Ramponi, E. Dieguez, M. Ferrari, and M. Mattarelli; Optical properties of Dy^{3+} doped yttrium-aluminum borate; Journal of Physics: Condensed Matter; Vol. 16; pp 465-471; 9 January 2004.
- [17] Huaidong Jianng, Jing Li, Jiyang Wang, Xiao-Bo Hu, Hong Liu, Bing Teng, Cheng-Qian Zhang, Peter Dekker, and Pu Wang; Growth of $\text{Yb}:\text{YAl}_3(\text{BO}_3)_4$ crystals and their optical and self-frequency-doubling properties, Journal of Crystal Growth, Vol. 233, pp 248-252, 2001
- [18] Amnon Yariv, Optical Electronics in Modern Communications, Oxford University Press, 5th edition, March 1, 1997.
- [19] Eric Black, Notes on the Pound-Drever-Hall technique; Laser Interferometer Gravitational Wave Observatory, Technical Note LIGO-T980045- 00- D, 16 April 1998.
- [20] T. W. Hansch, B. Couillaud; Laser Frequency Stabilization by Polarization Spectroscopy of a Reflecting Reference Cavity, Optical Communications, Vol. 35, pp 441-444, Dec. 1980.
- [21] K. J. Kuhn, Laser Engineering, Prentice-Hall Inc., 1998.
- [22] Castech <www.castech.com>, 2005-2007.
- [23] Yusuke Mori, Ikuo Kuroda, Satoshi Naakajima, Takatomo Sasaki, and Sadao Nakai; New nonlinear optical crystal: Cesium lithium borate, Applied Physics Letters, Vol. 65, 25 Sep 1995.
- [24] John B. Gruber, Thomas A. Reynolds, Douglas A. Keszler, and Bahram Zandi; Spectroscopic properties of nonlinear $\text{NdSc}_3(\text{BO}_3)_4$, Journal of Applied Physics, Vol. 87, pp 7159-7163; 15 May 2000.

Appendix A: Sellmeier Equations for given Materials.

Material	n_o	Ref.
Nd:YAB	$n_o^2 = 1 + \frac{172.4727}{\left(\frac{1}{0.1098684}\right)^2 - \left(\frac{1}{\lambda^2}\right)}$	[4]
Yb:YAB	$n_o^2 = 3.1762 + \frac{0.0013}{(\lambda^2 - 0.1480)} - 0.0971 \cdot \lambda^2$	[17]
Dy:YAB	$n_o^2 = 3.12691 + \frac{0.00935}{(\lambda^2 - 0.10234)} - 0.02893 \cdot \lambda^2$	[16]
BBO	$n_o^2 = 2.7359 + \frac{0.01878}{(\lambda^2 - 0.01822)} - 0.01354 \cdot \lambda^2$	[22]
CLBO	$n_o^2 = 2.208964 + \frac{0.010493}{(\lambda^2 - 0.012865)} - 0.011306 \cdot \lambda^2$	[23]
KD*P	$n_o^2 = 1.957554 + \frac{0.2901391 \cdot \lambda^2}{(\lambda^2 - 0.0281399)} - 0.02824391 \cdot \lambda^2 - 0.004977826 \cdot \lambda^4$	[22]

Material	n_e	Ref.
Nd:YAB	$n_e^2 = \frac{1}{\left(\frac{1}{0.1067225}\right)^2 - \left(\frac{1}{\lambda^2}\right)}$	[4]
Yb:YAB	$n_e^2 = 2.8632 + \frac{0.0090}{(\lambda^2 - 0.0937)} - 0.0083 \cdot \lambda^2$	[17]
Dy:YAB	$n_e^2 = 2.85717 + \frac{0.01197}{(\lambda^2 - 0.05894)} - 0.01091 \cdot \lambda^2$	[16]
BBO	$n_e^2 = 2.3753 + \frac{0.01224}{(\lambda^2 - 0.01667)} - 0.01516 \cdot \lambda^2$	[22]
CLBO	$n_e^2 = 2.058791 + \frac{0.008711}{(\lambda^2 - 0.011393)} - 0.006069 \cdot \lambda^2$	[23]
KD*P	$n_e^2 = 1.5005779 + \frac{0.6276034 \cdot \lambda^2}{(\lambda^2 - 0.0131558)} - 0.01054063 \cdot \lambda^2 - 0.002243821 \cdot \lambda^4$	[22]

LBO:

$$n_x^2 = 2.45414 + \frac{0.011249}{(\lambda^2 - 0.01135)} - 0.014591 \cdot \lambda^2 - 0.000066 \cdot \lambda^4$$

$$n_y^2 = 2.53907 + \frac{0.012711}{(\lambda^2 - 0.012523)} - 0.01854 \cdot \lambda^2 - 0.0002 \cdot \lambda^4$$

$$n_z^2 = 2.586179 + \frac{0.013099}{(\lambda^2 - 0.011893)} - 0.017968 \cdot \lambda^2 - 0.000226 \cdot \lambda^4$$

Ref: [22].

